Universal high-fidelity quantum gates for spin qubits in diamond

Bartling, H. P.; Yun, J.; Schymik, K. N.; Van Riggelen, M.; Enthoven, L. A.; Van Ommen, H. B.; Babaie, M.; Sebastiano, F.; Taminiau, T. H.; More Authors

DOI
10.1103/PhysRevApplied.23.034052

Publication date
2025

Document Version
Final published version

Published in
Physical Review Applied

Editors' Suggestion

Universal high-fidelity quantum gates for spin qubits in diamond

H.P. Bartling,[1,2,†] J. Yun,[1,2,†] K.N. Schymik,[1,2] M. van Riggelen,[1,2] L.A. Enthoven,[1,3] H.B. van Ommen,[1,2] M. Babaie,[1,3,4] F. Sebastiano,[1,3] M. Markham,[5] D.J. Twitchen,[5] and T.H. Taminiau[1,2,*]

[1] *QuTech, Delft University of Technology, PO Box 5046, 2600 GA Delft, Netherlands*
[2] *Kavli Institute of Nanoscience Delft, Delft University of Technology, PO Box 5046, 2600 GA Delft, Netherlands*
[3] *Department of Quantum and Computer Engineering, Delft University of Technology, 2628 CJ Delft, Netherlands*
[4] *Department of Microelectronics, Delft University of Technology, 2628 CD Delft, Netherlands*
[5] *Element Six, Fermi Avenue, Harwell Oxford, Didcot, Oxfordshire, OX11 0QR, United Kingdom*

(Received 25 June 2024; revised 14 November 2024; accepted 27 January 2025; published 21 March 2025)

Spins associated to solid-state color centers are a promising platform for investigating quantum computation and quantum networks. Recent experiments have demonstrated multiqubit quantum processors, optical interconnects, and basic quantum error-correction protocols. One of the key open challenges towards larger-scale systems is to realize high-fidelity universal quantum gates. In this work, we design and demonstrate a complete high-fidelity gate set for the two-qubit system formed by the electron and nuclear spin of a nitrogen-vacancy center in diamond. We use gate set tomography (GST) to systematically optimize the gates and demonstrate single-qubit gate fidelities of up to 99.999(1)% and a two-qubit gate fidelity of 99.93(5)%. Our gates are designed to decouple unwanted interactions and can be extended to other electron-nuclear spin systems. The high fidelities demonstrated provide opportunities towards larger-scale quantum processing with color-center qubits.

DOI: 10.1103/PhysRevApplied.23.034052

I. INTRODUCTION

Solid-state color centers are a promising qubit platform for exploring quantum simulation, computation and networks [1]. Pioneering experiments include the demonstration of small quantum networks [2–5], control of quantum processors with up to ten qubits [6–9], the implementation of rudimentary quantum algorithms [10–14], and the benchmarking of fault-tolerant quantum error-correction codes [15–17].

One of the main challenges on the road to larger-scale quantum information processing is to further improve the fidelity of quantum gates. In the short term, the gate fidelity sets the attainable depth and complexity of quantum algorithms. In the longer term, error correction and fault tolerance can be used to overcome imperfections, provided that single- and two-qubit gate fidelities satisfy error thresholds [18–21]. These prospects have stimulated a wide variety of research aiming to design, characterize, and optimize high-fidelity quantum gates in various platforms [8,12,22–38].

For color center qubits, the state of the art is set by the nitrogen-vacancy (N-V) center in diamond, which can be used as a two-qubit system consisting of the N-V electron spin and the intrinsic ^{14}N nuclear spin [6,8,12,22–24]. High-fidelity single-qubit gates have been demonstrated for the N-V electron spin and were characterized by randomized benchmarking [22,23]. Recent work reported a high two-qubit electron-nuclear gate fidelity (99.92%) using gate designs that are tailored to the noise environment [24]. However, the employed method of subspace randomized benchmarking does not consider the full two-qubit system and provides an upper limit rather than a best estimate for the fidelity [24]. Additionally, that work did not include single-qubit gates on the nuclear-spin qubit, which are challenging to perform due to the always present electron-nuclear coupling.

Here, we design, optimize, and characterize a complete set of high-fidelity quantum gates on the two-qubit system formed by the N-V electron and nitrogen spins. We design gates that precisely decouple unwanted interactions between the two qubits, as well as between the qubits and the environment, and use gate set tomography (GST) [39,40] to obtain the process matrix for both single- and

*Contact author: T.H.Taminiau@TUDelft.nl
†These authors contributed equally to this work.

two-qubit gates in the full two-qubit space. We use these process matrices to systematically identify sources of gate errors and develop improved calibration methods. We then demonstrate high fidelities for all gates in the two-qubit space (single-qubit gates around $F = 99.94\%$ and two-qubit gate $F = 99.93(5)\%$). Additionally, we design and characterize single-qubit gates for specific cases in which one of the qubits is not actively used, and demonstrate a fidelity of 99.991(4)% for the electron-spin qubit and a fidelity of 99.999(1)% for the nitrogen-spin qubit. Finally, we compile a SWAP gate from the characterized gate set to illustrate how the information of the gate errors can be used to implement error-mitigation techniques. We use this SWAP gate to store quantum states in the nitrogen quantum memory for over 100 s. Our systematic optimization and high gate fidelities for a complete gate set provide a promising starting point towards larger-scale quantum systems based on color-center qubits.

II. SYSTEM: N-V ELECTRON-NITROGEN SPIN QUBITS

We consider a single N-V center in a type-IIa isotopically purified diamond at 4 K. We study the two-qubit register formed by the N-V electron spin and the nitrogen (^{14}N) nuclear spin, and consider the surrounding ^{13}C nuclear spins (concentration approximately 0.01%) and P1 center electron spins (concentration approximately 75 ppb) as sources of noise [Fig. 1(a)] [41,42]. The Hamiltonian of this system is [43]

$$H = DS_z^2 + \gamma_e B_z S_z + \gamma_e B_\perp S_x + QI_z^2 + \gamma_n B_z I_z + \gamma_n B_\perp I_x + A_{xx} S_x I_x + A_{yy} S_y I_y + A_{zz} S_z I_z, \quad (1)$$

where $D \approx 2.87$ GHz is the zero-field splitting of the electron spin, $\gamma_e = 2.8024$ MHz/G ($\gamma_n = -307.7$ Hz/G) is the gyromagnetic ratio of the electron (nitrogen) spin, $Q \approx -4.949$ MHz is the quadrupole splitting of the nitrogen spin and $[A_{xx}, A_{yy}, A_{zz}] \approx [2.68, 2.68, 2.188]$ MHz are the diagonal hyperfine components of the spin-spin interaction between the electron spin and the nitrogen spin (Note II within the Supplemental Material [44]). $[S_x, S_y, S_z]$ ($[I_x, I_y, I_z]$) are the spin-1 operators for the electron (nitrogen) spin. We work at an approximately aligned, external magnetic field of $B_z \approx 62.29$ G and $B_\perp \approx 0.41$ G (Appendix D). We choose two levels of each qutrit to encode a qubit: $m_s = \{0, -1\}$ and $m_I = \{0, -1\}$ for the electron and nitrogen spin, respectively [Fig. 1(b)]. We initialize and read out the N-V electron spin through resonant, optical excitation [45]. Before each experimental repetition, we prepare the N-V center in the negative charge state and the lasers on resonance with the N-V transitions [46]. To initialize the nitrogen spin, we swap the electron $m_s = 0$ state to the nitrogen in a two-step SWAP initialization process (Appendix G). To read out the nitrogen spin, we map its spin state on the electron spin, which is then read out optically (Appendix H).

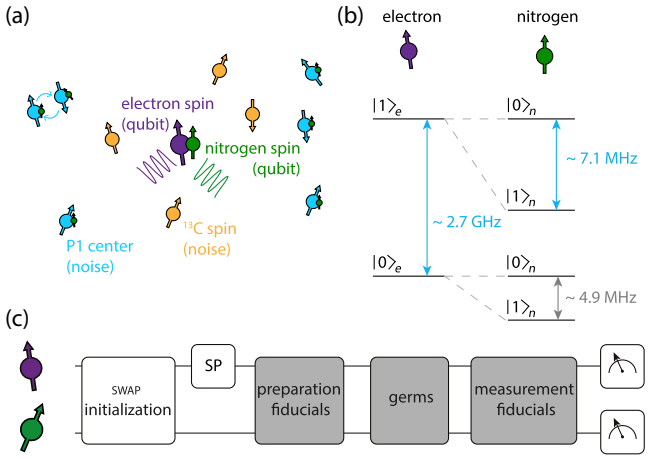

FIG. 1. System and experiment overview. (a) The system under consideration is the N-V center in diamond. The electron spin-1 (purple) and ^{14}N spin-1 (green) are surrounded by two spin baths that generate noise: nuclear ^{13}C spins and P1-center electron spins. (b) Schematic level diagram of the electron and nitrogen spin. The transitions indicated in blue are used for the electron and nitrogen gates. (c) Experimental implementation of gate set tomography. We initialize the nitrogen spin via a SWAP with the electron spin (Appendix G), after which we reinitialize the electron spin optically (SP = spin pump). Then, we run a set of preparation circuits (fiducials), germs, and measurement circuits, after which the electron and nitrogen spin are read out. The germs are longer sequences of gates meant to amplify specific types of errors [39,40].

III. GATE SET TOMOGRAPHY (GST)

To characterize and optimize gates, we use gate set tomography (GST). GST is a calibration-free tomography method used to characterize an informationally complete set of quantum gates [39,40]. It has previously been applied on a variety of systems, such as ion traps [47,48], quantum dots [28], silicon donors [29,49], and superconducting qubits [50]. The process entails executing a set of quantum circuits, consisting of preparation and measurement circuits (called fiducials) and germs that are used to amplify specific types of gate errors [Fig. 1(c)]. Compared to benchmarking methods, such as randomized benchmarking [51–56], interleaved randomized benchmarking [53,57,58], and cross-entropy benchmarking [59,60], GST estimates the complete process matrices for the gate set. In this work, we exploit that detailed information of the gate errors to systematically characterize and optimize gates for the electron-nitrogen two-qubit system.

IV. COMPLETE TWO-QUBIT GATE SET

A universal set of quantum gates requires a two-qubit gate, as well as single-qubit gates for each qubit. Note

that, in general, one is interested in the complete evolution within the two-qubit space. That is, a single-qubit rotation on one of the qubits should simultaneously realize the identity operation on the other qubit. For example, a single-qubit $\pi/2$ gate on the nitrogen nuclear spin is defined as $I_e \otimes R_x(\pi/2)_n$, with I_e the identity matrix.

A key challenge is that the electron- and nitrogen-spin qubits have an "always-on" hyperfine interaction [Eq. (1)], and that the electron spin continuously couples to the surrounding spin bath. Therefore, a central element of this work is to design composite gates that can precisely decouple unwanted interactions during the gate operations.

In specific cases, the conditions for single-qubit gates can be relaxed. For example, when at a given moment in an algorithm the other qubit is in a known computational eigenstate or its information does not need to be preserved, some interactions do not have to be decoupled. Below, we first consider the general case of the full two-qubit space. We discuss single-qubit gates optimized for specific cases in a later section.

As basic operations on the electron-spin qubit we use π- and $\pi/2$-pulses, which we implement by applying Hermite pulse shapes modulated by the electron-spin frequency (approximately 2.7 GHz). A Hermite pulse shape is chosen to minimize the effects of the detunings introduced by the different nitrogen-spin states (Appendix E).

Out of these π- and $\pi/2$-pulses, we construct composite $\pi/2$ and identity gates [Fig. 2(a)]. All gates include dynamical decoupling of the electron spin in order to avoid phase errors due to the electron-nitrogen interaction

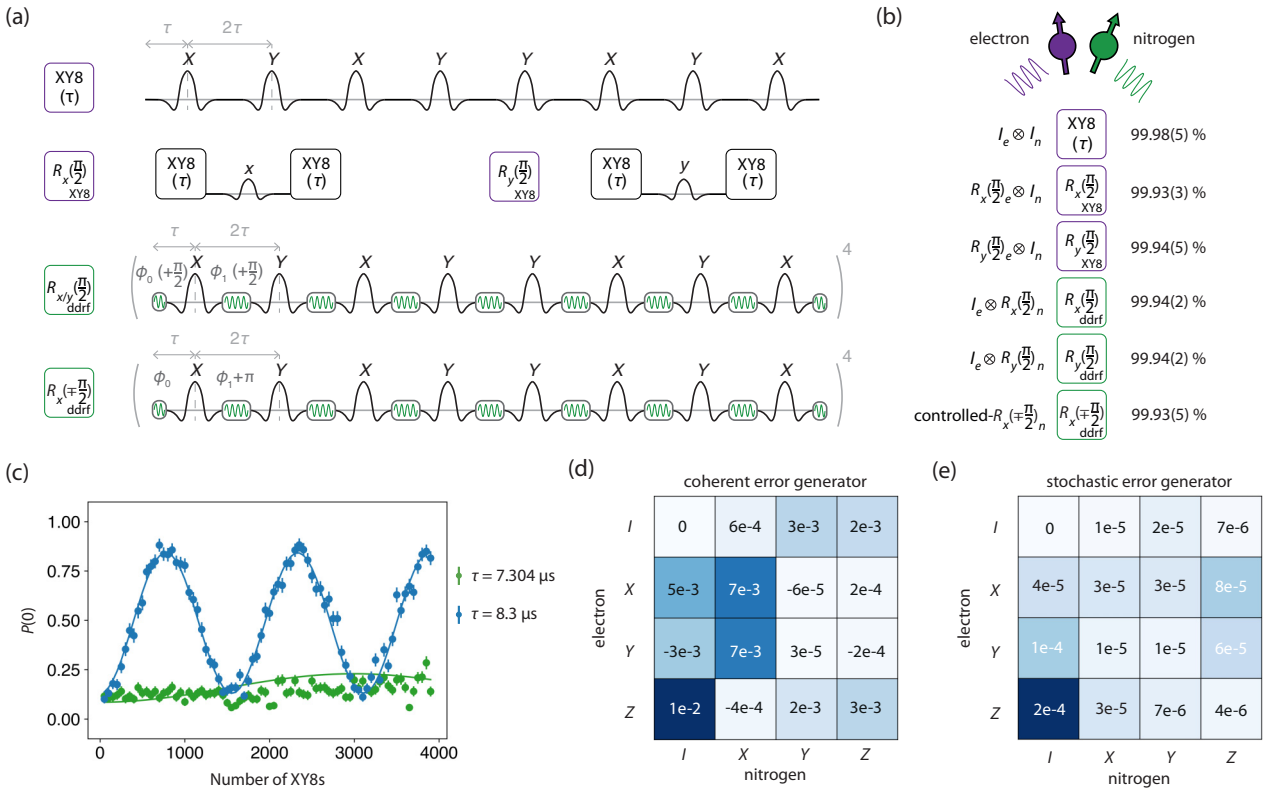

FIG. 2. Two-qubit GST on the electron-nitrogen system. (a) Pulse sequences for the electron, nitrogen, and two-qubit gates. The identity operation is implemented by an XY8 decoupling sequence. The electron $\pi/2$-pulses are placed between XY8 sequences. The nitrogen single-qubit gates are implemented using DDRF [6]. For the two-qubit gate, all odd rf pulses get an additional π phase shift, which makes the nitrogen rotation conditional on the electron-spin state. (b) Average gate fidelities for the electron-nitrogen two-qubit system (Appendix C for the definition of average gate fidelity). For each operation (left), we show the gate implementation [middle, see (a)] and the average gate fidelity (right). The single-qubit gate fidelities take into account the effect on the other qubit (Appendix C). The error bars represent one standard deviation (a 67% confidence interval). (c) Effect of the XY8 dynamical-decoupling sequence ($I_e \otimes I_n$) of (a) on the nitrogen spin for different interpulse delays τ. We initialize the nitrogen spin in $m_I = 0$ and apply a variable number of XY8 sequences with $\tau = 7.304$ μs (green) or $\tau = 8.3$ μs (blue). We find a coherent rotation of the nitrogen spin at $\tau = 8.3$ μs whereas this is absent for $\tau = 7.304$ μs. The blue line for $\tau = 8.3$ μs is a fit that yields the perpendicular magnetic field $B_\perp \approx 0.41$ G (Appendix D). The green line for $\tau = 7.304$ μs is a simulation of the expected signal given the extracted $B_\perp$. The error bars on the data represent one standard deviation. (d),(e) Coherent and stochastic error generators for the controlled gate ($R_x(\mp\pi/2)$). The box colors are proportional to the magnitude of the indicated values. Dephasing of the electron spin (stochastic, $Z \otimes I$) is the main contribution to the average gate infidelity.

[predominantly of the form S_zI_z, see Eq. (1)], and to decouple from the environment. To optimize the electron gates, we calibrate the interpulse delay τ, as well as the amplitude of the electron π- and $\pi/2$-pulses for both the gates around x and y (Appendix K).

To implement gates involving the nitrogen spin, we use dynamical decoupling radio-frequency (DDRF) gates [6]. The DDRF gate consists of dynamical decoupling on the electron spin interspersed with rf pulses (approximately 7.1 MHz) on the nitrogen-spin qubit [Fig. 2(a)]. This decouples the electron spin from its environment while simultaneously driving the nitrogen spin. By updating the phases between consequent rf pulses to account for the nitrogen-spin precession, an effective rotation builds up. By shifting the overall phase of the rf pulses, we can rotate the nitrogen spin around either x or y.

This rotation can be chosen to be unconditional (a single-qubit gate) or conditional on the electron-spin state (a two-qubit gate), by setting the phases of the rf pulses [6]. This conditional interaction is a controlled $\mp\pi/2$ gate around x:

$$|0\rangle\langle 0|_e \otimes R_x(-\pi/2)_n + |1\rangle\langle 1|_e \otimes R_x(\pi/2)_n, \qquad (2)$$

where 0 (1) refers to the electron-spin qubit being in $m_s = 0$ ($m_s = -1$). To optimize the nitrogen gates, we apply multiple, consecutive $\pi/2$ gates, while sweeping the rf amplitude of the DDRF gates (Appendix K). No separate optimization is performed for the two-qubit gate.

After optimization (see below for an extended discussion), we observe single-qubit gate fidelities around 99.94% and a two-qubit gate fidelity of 99.93(5)% for full two-qubit operation [Fig. 2(b), see Appendix C for the definition of average gate fidelity]. These fidelities are amongst the highest reported in any system [27,28,31,32,35,37,38]. Compared to a previous characterization of different N-V-center gates using subspace randomized benchmarking [24], the fidelities we obtain are best-estimates rather than upper limits, we obtain the full process matrices, and we implement a complete gate set that includes nitrogen-spin single-qubit gates.

To investigate the stability of the system and the robustness of the calibration routines, we perform a total of four two-qubit GST experiments. Across all experiments, we consistently find fidelities above 99.9% for all gates. The two-qubit gate fidelity averaged over the four runs is $F_{\text{avg}} = 99.923 \pm 0.026\%$ (Note V within the Supplemental Material [44]).

V. GATE OPTIMIZATION

Our starting point were the DDRF gates and calibration steps as introduced in Bradley *et al.* [6]. We then used GST and the resulting model violation and process matrices to systematically identify previously overlooked sources of noise and calibration errors. The main improvements made are as follows: (1) Improved calibration of the microwave and rf pulse amplitudes by embedding the pulses in XY8 sequences, in order to remove non-Markovianity and enabling consistent concatenation of the full gate set (Appendix F), (2) precise calibration of the the I and Q modulation channels for the electron pulses, and (3) setting the interpulse delay τ and the magnetic-field strength, according to conditions we derive below, to decouple the electron spin from the environment and the ^{14}N spin, while simultaneously avoiding spurious unconditional rotations of the ^{14}N spin. We now describe the latter point in more detail.

A key gate optimization step is to set the interpulse delay τ of the electron XY8 decoupling sequence. Ideally, this sequence cancels the interaction of the electron-spin qubit with the spin environment and with the nitrogen-spin qubit, performing an identity gate on both qubits. However, such decoupling sequences can resonantly couple the N-V electron-spin qubit to the dynamics of the surrounding spin bath, which includes the dynamics of individual nuclear spins [42,61–63], as well as of nuclear-spin pairs [64] and electron-spin pairs [65]. We leverage our detailed knowledge of the nuclear- and electron-spin environment of this N-V center [41,42,65] to choose suitable values of the interpulse delay τ, at which we avoid decoherence of the electron spin due to the ^{13}C and P1 spin baths (Appendix D).

Next, we optimize the electron XY8 decoupling sequence for performing the identity operation on the nitrogen-spin qubit. To remove residual z rotations we set τ to a multiple of the period set by the average precession frequency of the nitrogen spin for the two electron states ($\tau = 4\pi n/(\omega_0 + \omega_{-1})$).

However, for this value of τ, we observe a small but significant unconditional coherent rotation on the nitrogen-spin qubit for the electron XY8 decoupling sequence [Fig. 2(c)]. This coherent rotation can be explained by an effective S_zI_x interaction [61,66] between the electron and nitrogen spin coming from the misaligned magnetic field of $B_\perp \approx 0.41$ G, which breaks the symmetry of the system (Appendix D) [66].

To remove this nitrogen-spin rotation, we impose a second condition: $\tau = 2\pi m/(\omega_0 - \omega_{-1})$. Together with the first condition, this ensures that a single dynamical decoupling unit $(\tau - \pi - 2\tau - \pi - \tau)$ does not induce any effective rotation on the nitrogen-spin qubit, independent of the exact field alignment [Fig. 2(c), Appendix D]. This design makes the gate robust to magnetic-field misalignment.

VI. GATE ERRORS

GST provides completely positive trace-preserving process matrices for the gate set [39,40]. Since the process

matrix offers a complete description of the two-qubit evolution under the action of a gate, it provides information about the type, origin, and magnitude of infidelities in our system. Error generators can be used to dissect the process matrices in distinct error sources with clear physical interpretations [40]. In particular, the coherent Hamiltonian and the incoherent stochastic error generators distinguish between unitary error processes, such as over- and under-rotations, and stochastic error processes, such as qubit dephasing.

For the two-qubit gate, the largest remaining error source is the electron single-qubit coherent error around z [Fig. 2(d)]. However, coherent errors only contribute quadratically to the average gate fidelity, whereas stochastic errors contribute linearly [47,67,68]. Therefore, we conclude that the average gate fidelities of the gates in this work are mainly limited by single-qubit dephasing ($Z_e I_n$) and single-qubit bit flips ($Y_e I_n$) of the electron-spin qubit (Note VII within the Supplemental Material [44]).

The electron-spin dephasing and bit flips likely originate from magnetic-field noise. The main candidates for the source are the fluctuating external magnetic field and the spin environment of the N-V center [Fig. 1(a)]. The timescale of the noise plays an important role in its effect on the gates. Simulations show that quasistatic noise, which fluctuates slowly and can be considered as constant during a single gate, has no significant effect on the gate fidelity due to the XY8 decoupling sequences (Appendix F). However, higher-frequency noise, which fluctuates within a single gate, may explain the observed electron-spin dephasing and bit flips. A likely source are the spin-bath dynamics, in particular, flip-flops (approximately kHz) of interacting P1 centers (approximately 75 ppb) [41,65].

VII. CONTEXT-SPECIFIC SINGLE-QUBIT GATES

For both single- and two-qubit gates, the two-qubit process matrix is the most complete description (Fig. 2). However, gates optimized using two-qubit process matrices are not necessarily optimal under all circumstances. For example, if one qubit is in a well-defined state (e.g., an eigenstate) or does not hold valuable information and is allowed to dephase, then more optimal or simpler single-qubit gate designs likely exist for the other qubit. Such situations are very common in quantum algorithms, for example, in quantum error correction where ancillary qubits are regularly measured and reinitialized [63]. In what follows, we consider various single-qubit gate designs and their performance in different cases. To characterize these gates, we perform GST on the single-qubit system of either the electron-spin or nitrogen-spin qubit.

We first consider single-qubit gates on the electron spin for the specific case in which the nitrogen spin is in a known eigenstate. In this case, it is not necessary to decouple the hyperfine coupling, so that a gate consisting of a simple microwave pulse can be used [Fig. 3(a)]. Figure 3(b) (left) shows the gate fidelities from GST for $m_I = 0$. Compared to the gate designs with decoupling

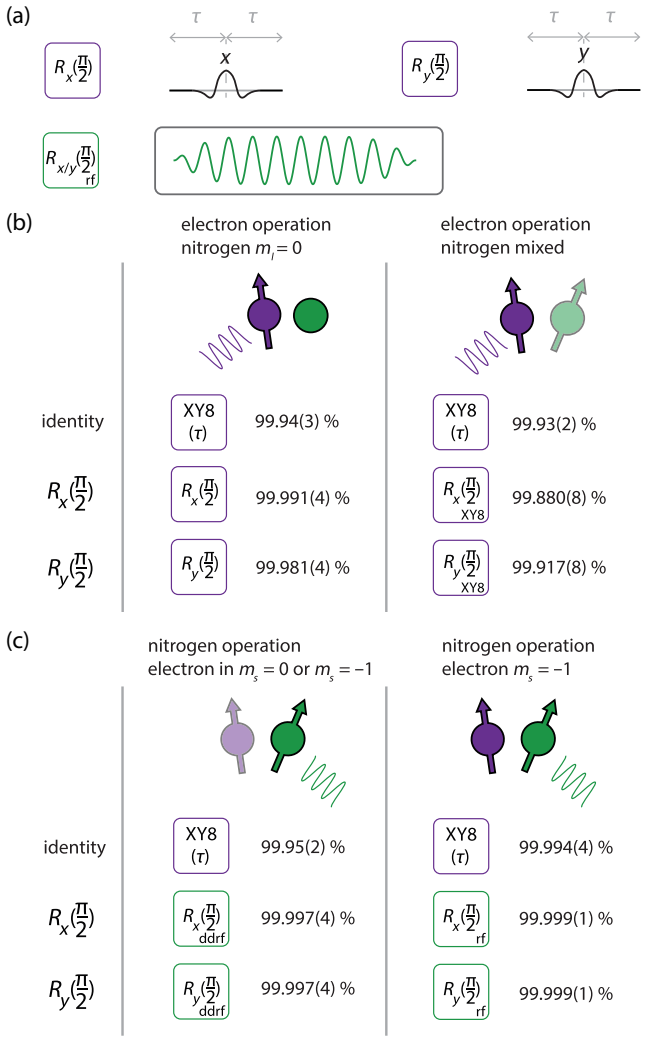

FIG. 3. Single-qubit GST for the electron-spin and nitrogen-spin qubits. (a) Pulse sequences. We additionally implement single-qubit gates without XY8 decoupling for the electron-spin qubit and for the nitrogen-spin qubit (rf pulses; length approximately 100 μs; risetime 1 μs). (b) Average gate fidelities from single-qubit GST for the electron-spin qubit for two different cases. (Left) The nitrogen spin is in $m_I = 0$ and the $\pi/2$ gates do not include XY8 decoupling. (Right) The nitrogen spin is mixed and the $\pi/2$ gates include XY8 decoupling. (c) Average gate fidelities from single-qubit GST for the nitrogen-spin qubit, for two cases. (Left) The $\pi/2$ gates are implemented using DDRF, which can be used regardless of the electron-spin state. Here, the electron spin is in $m_s = 0$. In Note IV within the Supplemental Material [44] we show the result for $m_s = -1$, obtaining similar fidelities. (Right) The $\pi/2$ gates are implemented using simple rf pulses (no decoupling), with the electron-spin state being $m_s = -1$. For (b) and (c), the error bars represent one standard deviation (a 67% confidence interval).

(Note IV within the Supplemental Material [44]), we find a slight improvement in fidelity, which we attribute to the removal of the XY8 decoupling sequences. Additionally, the direct microwave pulse is much faster (1.344 μs vs 234.728 μs) and reduces the stochastic gate errors, so that it is preferred when the nitrogen spin is in a known eigenstate during algorithms.

Next, we consider the case where the nitrogen spin is fully mixed ($m_I = 0, \pm 1$). This case applies when the nitrogen spin is not (yet) used in an algorithm, which is common, for example, during sensing experiments or remote entanglement generation [2–4]. In this case, the strong hyperfine coupling makes it preferable to apply decoupling, and the simple microwave pulse [Fig. 3(a)] shows significantly lower fidelity (approximately 99.86%, Note IV within the Supplemental Material [44]). Figure 3(b) (right) shows that the fidelities for the gates with decoupling are slightly reduced compared to the pure nitrogen-spin state, as the hyperfine interaction ($A_{zz} \approx 2.188$ MHz) combined with the limited peak Rabi frequency ($\Omega \sim 27$ MHz) cause different electron-spin rotations for the three nitrogen states (Appendix E).

For the nitrogen-spin qubit, we first characterize the DDRF-based single-qubit gates [Fig. 2(a)] in the single-qubit subspace for different electron-spin states [Fig. 3(c) and Note IV within the Supplemental Material [44]]. We find fidelities of 99.997(4)%, confirming that the gate fidelity in the two-qubit subspace is mainly limited by errors on the electron spin. When the electron is in a known eigenstate (here $m_s = -1$), the nitrogen-spin gates can alternatively be implemented by a simple rf pulse [Fig. 3(a)] at the corresponding frequency (approximately 7.1 MHz), without decoupling. We introduce a risetime of 1 μs and additionally we match the pulse length (∼100 μs) to be a multiple of the nitrogen-spin precession frequency to avoid any effective z rotation. For this case, we observe fidelities of 99.999(1)% [Fig. 3(c)], limited by the measurement uncertainty. These gates outperform the DDRF-based single-qubit gates, for the specific case where the electron spin is in an eigenstate, and the fidelities obtained are among the highest single-qubit gate fidelities reported on any platform [22,27,28,37,69–73].

To explicitly demonstrate a universal gate set, we also implement a T gate (or $\pi/4$ gate) for both the electron-spin and nitrogen-spin qubit using the gate designs that include XY8 decoupling [as in Fig. 2(a)]. We characterize the T gates in the single-qubit subspace (Note IV within the Supplemental Material [44]). For the electron-spin qubit, we find an average gate fidelity of $F = 99.989(7)\%$, and for the nitrogen-spin qubit we find $F = 99.986(6)\%$.

For comparison, we also perform single-qubit randomized benchmarking [51,53] on the electron $\pi/2$ gates with and without XY8 decoupling, as well as on the nitrogen DDRF $\pi/2$ gates. We compare the average fidelity from randomized benchmarking to simulations based on the process matrices obtained from GST (Appendix M). We generally find good agreement between the two methods, with small deviations likely originating from the presence of non-Markovian noise [47]. A detailed analysis is given in Appendix M.

VIII. SWAP GATE IMPLEMENTATION

The two-qubit process matrices from GST provide a complete characterization, which can be used to predict the outcome of any gate sequence or algorithm on the two qubits. In principle, for the two-qubit system, no other gate sequences need to be investigated. Nevertheless, it is instructive to consider the compilation of extended circuits and algorithms from the characterized gate set. In particular, the effect of coherent errors [Fig. 2(d)] and their suppression by error-mitigation methods depends on the specific sequences of gates in an algorithm.

As an example, we choose to implement an electron-nitrogen SWAP gate and use it to swap quantum states from and to the nitrogen-spin qubit, which provides a long-lived quantum memory. We construct a single SWAP gate using a total of 17 gates from the characterized gate set [Fig. 4(a)]. Note that a SWAP operation can be compiled with fewer gates, but this choice allows us to validate the predictive power of the obtained GST process matrices. From the two-qubit process matrices, we obtain an expected SWAP gate fidelity of 98.7%.

To investigate the SWAP gate, we repeatedly apply it, swapping a quantum state between the two qubits [Fig. 4(b)]. We apply the SWAP sequence an even number of times with the electron spin prepared along each of its cardinal axes. After about 20 SWAP gates, the resulting average state fidelity reaches 0.5. The prediction using the process matrices obtained with GST is in good agreement with the experimental results, even up to approximately 800 elementary gates (Appendix N), indicating that the GST model and its assumptions are accurate.

Next, we theoretically analyze the limitations of the SWAP gate using the error generators [Figs. 2(d) and 2(e)]. The main source of the observed decay are coherent errors that build up by repeatedly applying the SWAP gate. Upon theoretically excluding the coherent errors from the process matrices, a much slower decay is predicted, going well beyond 150 SWAP gates [Fig. 4(b)]. Removing all coherent errors is not easily achieved experimentally. However, based on the explicit knowledge of the coherent error processes, tailored sequences might be designed to cancel their effect. A simple example is to add an inversion π gate (two extra electron $\pi/2$ gates) between every SWAP gate, which cancels part of the accumulation of coherent errors [Fig. 4(b)]. Alternatively, error-mitigation techniques such as Pauli twirling [18,51,74,75] can be used to prevent coherent errors from adding up (see the analysis in Appendix O).

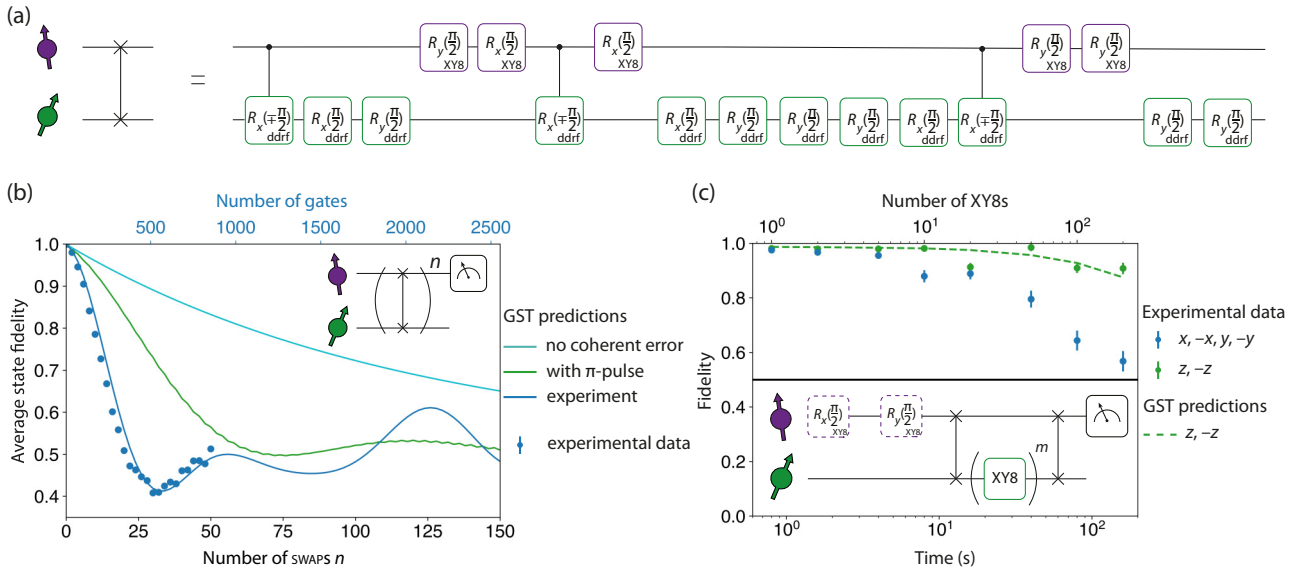

FIG. 4. Implementation of an electron-nitrogen SWAP gate. (a) Sequence to perform an electron-nitrogen SWAP gate composed of the gates characterized by two-qubit GST (Fig. 2). The compiled sequence is not generally optimal, but demonstrates the utility of GST in predicting the action of extended circuits. (b) Application of n sequential SWAP gates. The experimental data (blue points) are predicted well by the GST process matrices (blue line). The GST predictions without any coherent error (cyan) and with an additional π-pulse between sequential SWAP gates (green) are also shown. The error bars are smaller than the data points. (c) Storage of all six electron cardinal states ($\pm x, \pm y, \pm z$) on the nitrogen spin with the SWAP gate, showing the protection of a quantum state for over 100 s. We compare the experimental data for $\pm z$ to the GST prediction that does not include any free evolution. We find that the $\pm z$ decay is well explained by the obtained process matrix and thus likely caused by gate imperfections. For the experimental data for $\pm x, y$, it is not possible to predict the signal from just the obtained process matrices, as the GST process did not include the (varying) free-evolution time. The nitrogen XY8 decoupling is implemented with the DDRF $\pi/2$ gates around x and y characterized by two-qubit GST (Fig. 2). The error bars on the data represent one standard deviation.

The example in Fig. 4(b) underlines the limitation of using a single number as a metric of the quality of a gate. The average gate fidelity captures the effect of decoherence during the gates properly. However, if unitary errors build up or cancel in a compiled circuit, it becomes impossible to predict the error rate from the average gate fidelity alone [68]. Process matrices obtained with GST, on the other hand, predict the behavior of such compiled circuits accurately and can be used to design optimized subroutines (Appendix N).

Finally, as an example of a potential application for the SWAP gate, we use the nitrogen-spin qubit as a quantum memory to temporarily store an arbitrary quantum state. First, we prepare the electron spin in one of six cardinal states and swap the state to the nitrogen-spin qubit. Then, we apply XY8 dynamical decoupling on the nitrogen-spin qubit using the GST-characterized DDRF $\pi/2$ gates. We measure the average state fidelity of the nitrogen spin as a function of the number of XY8 decoupling sequences [Fig. 4(c)]. We find that the quantum state on the nitrogen spin can be maintained for over 100 s, showing its promise as a quantum memory (see also Ref. [6]).

We compare the experimental data with a simulation based on the two-qubit GST process matrices (without the inclusion of a free-evolution time). From this simulation, we find that the errors in the nitrogen DDRF $\pi/2$ gates can explain the decay of the nitrogen $\pm z$ eigenstates [Fig. 4(c)]. Additionally, we find that the electron-spin population decays at a timescale similar to the decoherence of the nitrogen $\pm x$ and $\pm y$ states (Appendix P). This suggests that the current measurement is limited by gate imperfections that affect the electron-spin population, and that longer coherence times are likely achievable by using the gates of Fig. 3, but this is not pursued here.

IX. CONCLUSION

In conclusion, we have designed, characterized, and systematically optimized a universal set of single- and two-qubit gates on the electron-nitrogen spin system of the N-V center using gate set tomography. A central element of the gate design and optimization is to precisely decouple the (unwanted) effects of the electron-nitrogen hyperfine interaction. We have demonstrated single-qubit gate fidelities of up to 99.999(1)% and a two-qubit gate fidelity of 99.93(5)%. These are among the most accurate quantum gates shown on any platform [22,24,27,28,31,32,35,37,38,69–73], and present a step towards enabling larger-scale algorithms.

Future work might further improve the gates by targeting the dominant error generators identified here [Figs. 2(d) and 2(e)]. Additionally, improved fidelities for initialization, readout and (photon-mediated) electron-electron two-qubit gates will be required for large-scale quantum information processing. The methods developed here provide a starting point for optimizing gates for a variety of colour centers in various materials, including diamond, silicon carbide, and silicon [76–78], as well as for gates in multiqubit systems [6,17].

ACKNOWLEDGMENTS

We thank R.J. Blume-Kohout, C.I. Ostrove, J. Gonzalez de Mendoza, M. Rimbach-Russ, J. Borregaard for valuable discussions. We gratefully acknowledge support from the joint research program "Modular quantum computers" by Fujitsu Limited and Delft University of Technology, co-funded by the Netherlands Enterprise Agency under project number PPS2007. This work was supported by the Netherlands Organisation for Scientific Research (NWO/OCW) through a Vidi grant, as part of the Frontiers of Nanoscience (NanoFront) programme and through the project "QuTech Phase II funding: "Quantum Technology for Computing and Communication" (Project No. 601.QT.001). This project has received funding from the European Research Council (ERC) under the European Union's Horizon 2020 research and innovation programme (Grant Agreement No. 852410). This project has received funding from the European Union's Horizon Europe research and innovation program under Grant Agreement No. 101135699. This work was supported by the Dutch National Growth Fund (NGF), as part of the Quantum Delta NL programme. This work is part of the research programme NWA-ORC (NWA.1292.19.194), which is partly financed by the Dutch Research Council (NWO). This research was supported by the education and training program of the Quantum Information Research Support Center, funded through the National Research Foundation of Korea (NRF) by the Ministry of Science and ICT (MSIT) of the Korean government (No. 2021M3H3A103657313). The fitting algorithms were performed on the DelftBlue supercomputer at Delft University of Technology [79].

H.P.B., J.Y., and T.H.T. devised the experiments. H.P.B., J.Y., K.N.S., and M.v.R. performed the experiments and collected the data. H.P.B., J.Y., K.N.S., M.v.R., L.A.E., and H.B.v.O. prepared the experimental apparatus. H.P.B., J.Y., K.N.S., M.v.R., L.A.E., H.B.v.O., M.B., F.S., and T.H.T. analyzed the data. M.M. and D.J.T. grew the diamond sample. H.P.B., J.Y., K.N.S., M.v.R., and T.H.T. wrote the manuscript with input from all authors. M.B., F.S., and T.H.T. supervised the project.

DATA AVAILABILITY

All data underlying the study are available on the open 4TU data server [80]. Code used for performing the numerical simulations is available on request.

APPENDIX A: EXPERIMENTAL DETAILS

1. Experimental setup and sample

The experiments are performed on a type-IIa isotopically purified (targeted 0.01% ^{13}C) ⟨100⟩ diamond substrate (Element Six). We use a home-built confocal microscope to address a single N-V center at 4 K. A solid immersion lens and antireflection coating are fabricated around the N-V center to increase the collection efficiency [46]. We use three orthogonal permanent NdFeB magnets mounted on linear actuators (Newport UTS100PP) to apply an external magnetic field aligned along the N-V symmetry axis. To initialize and read out the N-V electron-spin state, we use resonant optical excitation (Toptica DLPro and New Focus TLB-6704-P). We measure readout fidelities of 83.3(4)% for the $m_s = 0$ spin state and 98.9(1)% for the $m_s = -1$ spin state, obtaining an average readout fidelity of 91.1(2)%. To prepare the N-V in the N-V^- charge state and lasers on-resonance with the N-V^- transitions, we perform a charge-resonance check [46], which additionally involves 515-nm (green, Cobolt MLB) excitation. Through direct current modulation or cascaded acousto-optical modulators, we realize on-off ratios exceeding 100 dB for all lasers so that the electron-spin relaxation T_1 is negligible [63].

2. Microwave and rf driving

For electron-spin driving, we use single-sideband modulation at 250 MHz. The I and Q signals are generated on an arbitrary waveform generator (Tektronix AWG5014C), which modulates an rf source (R&S SGS100A). We use a 20-W amplifier (AR 20S1G4) to attain peak Rabi frequencies of approximately 27 MHz, followed by a microwave switch, which is shut when microwaves are not applied to protect the N-V from amplifier noise [81]. For nitrogen-spin driving, we generate the rf frequency directly from the arbitrary waveform generator. Finally, the electron-spin and nitrogen-spin driving signals are combined on a diplexer. For more details on the electronics, see Note I within the Supplemental Material [44].

3. Magnetic-field stabilization

To mitigate magnetic-field fluctuations, we intermittently (approximately every 10–20 min.) calibrate the electron-spin resonance frequency to within 2 kHz of the set point by moving one of the three permanent magnets. Due to this intermittent calibration, the typical peak-to-peak fluctuations of the electron-spin resonance frequency during the two-qubit GST experiments do not exceed 10 kHz.

TABLE I. Settings and model violation for the presented GST experiments. L is the maximum circuit depth, repetitions is the number of experimental repetitions per circuit and N_σ quantifies the model violation [39].

Fig. 2			
Name	L	Repetitions	N_σ
Full operation	128	1000	11.7
Fig. 3			
Name	L	Repetitions	N_σ
Electron operation nitrogen $m_I = 0$	128	1000	8.71
Electron operation nitrogen mixed	128	1000	15.4
Nitrogen operation electron 0 or -1	128	2000	1.3
Nitrogen operation electron $m_s = -1$	512	1000	2.76

APPENDIX B: DATA ANALYSIS

Here, we summarize the experimental settings and model violation for the presented GST results. We group the results per figure and indicate the corresponding name in that figure (Table I). First, we show the maximum circuit depth L used for that experiment. When we indicate $L = 128$, that implies that germs of depth $1, 2, 4, 8, 16, 32, 64$, and 128 were run [39]. Then, we indicate the experimental repetitions used for each circuit. The estimation error of gates in GST is typically of the order $O(1/(L\sqrt{N}))$ where N is the number of repetitions [39]. To perform the GST analysis, we use pyGSTi [82]. For the process matrix, we require complete positivity and trace preservation (CPTP). Lastly, we report the N_σ metric for $L = 128$, which quantifies the model violation [39]. The error bar on the average gate fidelities obtained with GST represent one standard deviation (a 67% confidence interval). Other important elements of the GST experiments are the preparation fiducials, germs, and measurement fiducials used. We provide these separately, together with the data.

APPENDIX C: AVERAGE GATE FIDELITY

In this work, we use the average gate fidelity as a metric to summarize the quality of each gate. The average gate fidelity is calculated by comparing the process matrix in the Pauli transfer matrix representation [83], obtained through gate set tomography, to the ideal target process matrix [67]:

$$F_{\text{avg}} = \frac{\text{Tr}(P_{\text{exp}}^{\dagger} P_{\text{target}})/d + 1}{d + 1}, \tag{C1}$$

where P_{exp} (P_{target}) is the process matrix for the experimental (ideal) gate in the Pauli transfer matrix representation such as [67]

$$(P_\Lambda)_{ij} = \frac{1}{d} Tr(\sigma_i \Lambda(\sigma_j)), \tag{C2}$$

where Λ is the map of the gate to be characterized, $\sigma_{i(j)}$ is the Pauli operator for axis i (j) and d is the dimension of the system of interest.

In this work, we primarily consider two-qubit GST and process matrices of dimensions 16×16 ($d = 4$, two-qubit space) (Figs. 2 and 4). In the section "Context-specific single-qubit gates" we use single-qubit GST, which only considers a single-qubit subspace, and thus process matrices of dimensions 4×4 ($d = 2$, single-qubit space) (Fig. 3). In the latter case, deviations from the identity process on the other qubit do not directly result in a reduced gate fidelity.

APPENDIX D: XY8 SEQUENCE: DECOUPLING THE ELECTRON-NUCLEAR INTERACTION

Our gate designs use dynamical decoupling sequences to decouple the interaction between the electron and nuclear spin, as well as the interactions of the electron spin with the surrounding spin baths and other noise sources. We then realize single- and two-qubit gates involving the ^{14}N nuclear spin by adding direct rf driving.

1. Decoupling from the ^{13}C and P1-center baths

During dynamical decoupling, the N-V electron-spin qubit can couple to single nuclear-spin dynamics [42,61–63], as well as electron- [65] and nuclear-spin [64] pair dynamics. In particular, we have previously demonstrated the control of a single ^{13}C spin [42] and of a single pair of P1 centers [65] surrounding this N-V center. To avoid decoherence of the N-V electron-spin qubit due to these nuclear and electron spins, we choose a suitable value of the interpulse delay τ. There is no observable interaction between the N-V electron spin and the P1-center pair for dynamical decoupling sequences below $\tau = 10\ \mu$s [65]. Additionally, at an external magnetic field of $B_z = 62.291(3)$ G, the interpulse delays τ at which the ^{13}C nuclear spins (concentration approximately 0.01%) couple coherently to the N-V electron-spin qubit are $\tau = (2k + 1)\tau_0$ where $\tau_0 = 1/(4\gamma_c B_z) \approx 3.75\ \mu$s. Together with the two other conditions (see below), this leads us to choose $\tau = 7.304\ \mu$s, at which τ we avoid coupling to the nuclear-spin bath and P1 electron-spin pairs.

2. Decoupling the electron-nitrogen interaction

Above, we considered the decoupling of the N-V electron-spin qubit from the environment. However, we also need to consider unwanted evolution of the nitrogen-spin qubit during the electron XY8 decoupling sequences, introduced by the hyperfine interaction. To minimize this, we satisfy two additional conditions for the interpulse delay τ in dynamical decoupling.

First, we set τ to a multiple of the period given by the average precession frequency of the nitrogen spin in

$m_s = 0$ and $m_s = -1$. Second, we set τ to a multiple of the period defined by the effective electron-nitrogen hyperfine interaction. That is, if ω_0 (ω_{-1}) is the precession frequency of the nitrogen spin when the electron spin is in $m_s = 0$ ($m_s = -1$), we set $\tau = 4\pi n/(\omega_0 + \omega_{-1})$ where n is an integer and simultaneously $\tau = 2\pi m/(\omega_0 - \omega_{-1})$ where m is an integer.

a. The first condition: $\tau = 4\pi n/(\omega_0 + \omega_{-1})$

The first condition ensures that the nitrogen spin undergoes a multiple of a 2π rotation around z for each gate. In this way, we minimize control errors around z. Due to a hardware constraint, τ is limited to multiples of 4 ns, which is relatively easy to satisfy when the average precession period is already a multiple of 2 ns. Therefore, we set the magnetic field such that the average precession frequency of the nitrogen spin is a multiple of 2 ns.

We adjust the magnetic field using the two electron-spin resonance frequencies: the transitions from $m_s = 0$ to $m_s = \pm 1$. This is an efficient way to approximately align the magnetic field by minimizing the sum of the $m_s = 0$ to $m_s = \pm 1$ transition frequencies [84]. Additionally, we move to a magnetic-field magnitude that satisfies the first condition described above: we set the magnetic field such that the period of the average nitrogen precession frequency is 166 ns (a multiple of 2 ns).

b. Nitrogen-spin rotation for $\tau = 4\pi n/(\omega_0 + \omega_{-1})$

After satisfying the first condition, we observe a coherent rotation of the nitrogen nuclear spin under dynamical decoupling of the electron spin (Fig. 5). This rotation of the nitrogen nuclear spin has been observed previously in the context of dc field sensing [66]. The slightly misaligned magnetic field in our system breaks the symmetry of the hyperfine interaction and induces an effective $A_{zx}S_zI_x$ interaction between the electron and nitrogen spin. This term then introduces a coherent rotation on the nitrogen spin when applying a dynamical decoupling sequence with

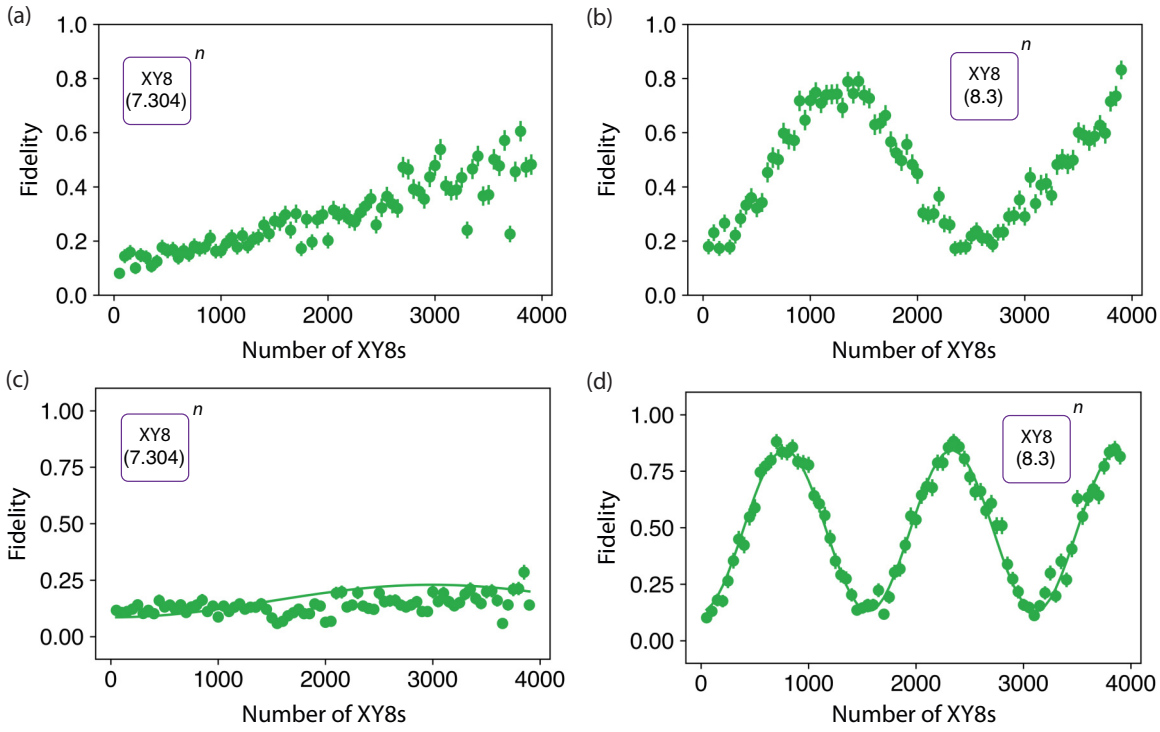

FIG. 5. Nitrogen rotation under electron XY8 decoupling for two different magnetic fields. (a) The nitrogen spin is initialized in $m_I = 0$ and under electron XY8 decoupling at $\tau = 7.304$ μs, we observe a slow rotation of the nitrogen spin. This indicates that the condition $\tau = 2\pi m/(\omega_0 - \omega_{-1})$ is not exactly matched for $\tau = 7.304$ μs. (b) Nitrogen rotation under electron XY8 decoupling at $\tau = 8.3$ μs. The reduced contrast compared to (d) indicates that the condition $\tau = 4\pi n/(\omega_0 + \omega_{-1})$ is not exactly matched for $\tau = 8.3$ μs and thus for $\tau = 7.304$ μs. (c) Nitrogen rotation under electron XY8 decoupling at $\tau = 7.304$ μs for an optimal external magnetic field. No rotation of the nitrogen spin under XY8 decoupling is observed, since $\tau = 7.304$ μs satisfies both conditions at this magnetic field: $\tau = 4\pi n/(\omega_0 + \omega_{-1})$ and $\tau = 2\pi m/(\omega_0 - \omega_{-1})$. (d) For the optimal magnetic-field setting, we observe a full-contrast rotation under decoupling at $\tau = 8.3$ μs. This happens because $\tau = 8.3$ μs is not a multiple of the effective electron-nitrogen interaction time ($\tau \neq 2\pi m/(\omega_0 - \omega_{-1})$), while it is a multiple of the period set by the average nitrogen-spin precession frequency ($\tau = 4\pi n/(\omega_0 + \omega_{-1})$). We fit the data in (d) to a simulation of XY8 decoupling on the system Hamiltonian, with $B_\perp$ as a free parameter (solid line). We find $B_\perp \approx 0.414$ G, which we then use to simulate the data in (c) (solid line).

a τ that satisfies the first condition, as is known from for example the control of ^{13}C nuclear spins [85]. Note that the effective A_{zx} coupling of the nitrogen under misaligned magnetic field was discussed in depth by Liu *et al.* [66]. For completeness, we summarize the related discussion here. The effective A_{zx} originating from a misaligned magnetic field is

$$A_{zx} = \frac{\gamma_e B_\perp A_\perp}{D - \gamma_e B_z} F, \tag{D1}$$

where $B_\perp$ is the off-axis magnetic field and $F \approx \frac{2\sqrt{2}(-Q+A_{zz}/2)^2}{(-Q+A_{zz})Q}$. These equations assume that the external magnetic field is such that the N-V center is close to the ground-state level-anticrossing (GSLAC), which is not satisfied in our work, rendering some approximations used in Ref. [66] quantitatively inaccurate. Compared to an N-V close to the GSLAC (see Ref. [66]), the nitrogen-spin rotation in this work is a more subtle effect that only appears when applying on the order of 1000 XY8 sequences (8000 π-pulses).

Under the presence of such an A_{zx} term, we can predict the rotation angle ϕ of the nitrogen spin per single dynamical decoupling unit consisting of $(\tau - \pi - 2\tau - \pi - \tau)$ using the following equation [61]:

$$\cos(\phi) = \cos(\alpha)\cos(\beta) - \cos(\theta)\sin(\alpha)\sin(\beta), \tag{D2}$$

where $\alpha = \omega_{-1}\tau$, $\beta = \omega_0\tau$, and θ is the angle between the two rotation axes of the nitrogen spin for the two different electron eigenstates ($m_s = 0$ and $m_s = -1$). The two rotation axes are obtained from the exact eigenstates we extract from the system Hamiltonian in Eq. (1).

c. The second condition: $\tau = 2\pi m/(\omega_0 - \omega_{-1})$

To avoid this unwanted rotation on the nitrogen-spin qubit, we require $\phi = 0$. To that end, either $\alpha = 0 \pmod{2\pi}$ and $\beta = 0 \pmod{2\pi}$ or $\alpha = \pi \pmod{2\pi}$ and $\beta = \pi \pmod{2\pi}$. In other words, we require $\alpha - \beta = 0 \pmod{2\pi}$. This can be rewritten to obtain the second condition outlined before: $\tau = 2\pi m/(\omega_0 - \omega_{-1})$.

Note that we can rewrite the two conditions ($\tau = 4\pi n/(\omega_0 + \omega_{-1})$ and $\tau = 2\pi m/(\omega_0 - \omega_{-1})$) as:

$$2\tau = \frac{2\pi(2n+m)}{\omega_0}, \tag{D3}$$

$$2\tau = \frac{2\pi(2n-m)}{\omega_{-1}}. \tag{D4}$$

There are two ways to satisfy these equations. The first type of solution is if τ is an integer multiple of the periods set by both ω_0 and ω_{-1}. This solution is obtained if $2n + m$ (and therefore $2n - m$) is an even number. Intuitively, in that case the evolution during a single τ equals the identity operation for both electron states and no nitrogen spin rotation can be created. For the second type of solution, $2n + m$ is odd (and therefore $2n - m$ is odd). In that case, the evolution during a single τ is an effective evolution of angle π, for both $m_s = 0$ and $m_s = -1$, which also becomes the identity operation for a full unit of the dynamic decoupling sequence $(\tau - \pi - 2\tau - \pi - \tau)$.

Because setting these conditions results in $\phi = 0$, the ^{14}N evolution becomes the identity operation, independent of the magnetic-field alignment. This choice of parameters thus makes the decoupling sequence—and by extension the gates in this work—intrinsically robust to magnetic-field misalignment.

3. Calibrating the magnetic field to minimize the nitrogen-spin rotation

The rotation of the nitrogen spin during XY8 decoupling was measured for two different values of τ: $\tau = 7.304$ μs and $\tau = 8.3$ μs. At the magnetic field obtained to satisfy the first condition for τ (Sec. D 2 a), $\tau = 7.304$ μs is already a close multiple of the effective electron-nitrogen interaction time, while $\tau = 8.3$ μs is not.

To measure the leftover rotation of the nitrogen spin at these values of τ, we apply many XY8 dynamical decoupling sequences with the nitrogen starting in $m_I = 0$ (Fig. 5). For a suboptimal external magnetic-field magnitude, we find that the nitrogen spin is rotated from $m_I = 0$ to $m_I = -1$ by an XY8 decoupling sequence at $\tau = 7.304$ μs [Fig. 5(a)]. Additionally, the nitrogen rotation present at $\tau = 8.3$ μs does not show full contrast [Fig. 5(b)]. We optimize the magnetic-field magnitude such that no nitrogen rotation is visible when decoupling at $\tau = 7.304$ μs [Fig. 5(c)] and a full-contrast nitrogen rotation is visible when decoupling at $\tau = 8.3$ μs [Fig. 5(d)]. This is equivalent to optimizing the magnetic field such that $\tau = 7.304$ μs satisfies both conditions: $\tau = 4\pi n/(\omega_0 + \omega_{-1})$ and $\tau = 2\pi m/(\omega_0 - \omega_{-1})$ with $n = 44$ and $m = 8$. This magnetic field ensures that no spurious nitrogen rotations are introduced at $\tau = 7.304$ μs by the XY8 decoupling. In Fig. 5(c) we verify that for our magnetic field we see no visible rotation of the nitrogen spin up to 4000 XY8 sequences on the electron spin (32 000 π pulses).

4. Magnitude of the magnetic-field misalignment

To investigate the required perpendicular magnetic field to reproduce this effect, we simulate the action of XY8 decoupling sequences on the electron-nitrogen spin system. We take the system Hamiltonian in Eq. (1) and simulate the effect of each π pulse using a time-dependent Hamiltonian propagator calculation as described in Note III within the Supplemental Material [44]. In Figs. 5(c) and 5(d), we show the simulation result for the nitrogen spin when a perpendicular magnetic field is present and

when τ is $100/(\omega_0+\omega_1) \approx 8.3$ μs and $88/(\omega_0+\omega_1) \approx 7.304$ μs. We fit to the experimental result for $\tau = 8.3$ μs in order to obtain $B_\perp$. We find $B_\perp = 0.41400000(1)$ G with a reduced chi-squared of the fit of $\chi_r^2 = 1.8$. Note that the confidence range of the perpendicular field is from the error of the fit, and the uncertainties on the coefficients within the Hamiltonian used in the model were not considered during the fit.

The simulations in Fig. 5 together with the data presented in Figs. 2 and 5 show that the conditions outlined above are required to avoid any coherent rotation of the nitrogen spin. In future experiments, the necessity of the first condition ($\tau = 4\pi n/(\omega_0+\omega_{-1})$) can be avoided through the use of more advanced phase-tracking methods.

APPENDIX E: GATE DESIGNS

In this section, we discuss some details of the electron and nitrogen pulses. We use a microwave frequency resonant with the $m_s = 0$ to $m_s = -1$ transition when $m_I = 0$. The main issue for the electron single-qubit gate is the relatively large interaction strength between the electron and nitrogen nuclear spin. Since the detuning induced by the coupling of the nitrogen spin (approximately 2 MHz) is comparable to our peak Rabi frequency (approximately 27 MHz), we use a Hermite envelope generated with the following formula:

$$f(t) = A\left(1-\eta\left(\frac{t-T_{\text{pulse}}/2}{0.1667T_{\text{pulse}}}\right)^2\right) \times \exp-\left(\frac{t-T_{\text{pulse}}/2}{0.1667T_{\text{pulse}}}\right)^2, \tag{E1}$$

where A is the amplitude of the Hermite envelope, η is a coefficient that is 0.956 (0.667) for a π- ($\pi/2$-)pulse and T_{pulse} is the defined pulse length (in this work, $T_{\text{pulse}} = 144$ ns) [86,87]. This makes it possible to rotate the electron spin similarly regardless of the nitrogen spin state. We can write the Hamiltonian of the N-V electron spin for a given nitrogen eigenstate m_I as

$$H_e = DS_z^2 + \gamma_e B S_z + m_I A_{zz} S_z, \tag{E2}$$

where $A_{zz} \approx 2.188$ MHz is the electron-nitrogen hyperfine interaction. If we now add a time-dependent Hamiltonian rotating at $D+\gamma_e B$ and move into the rotating wave frame of this frequency, the Hamiltonian after applying rotating wave approximation is

$$H_e = m_I A_{zz} S_z + \Omega_e(\cos(\phi)S_x + \sin(\phi)S_y). \tag{E3}$$

Thus the electron has a different detuning depending on the nitrogen-spin state. Therefore, when applying the same microwave pulse, the effective rotation is along a different rotation axis and has a different angle for different m_I. The Hermite envelope for the microwave pulse helps the phase accumulation during the microwave pulse to be more robust to detuning [86,87]. Figure 6(a) [6(a)] shows a simulation of the fidelity of a Hermite (square) $\pi/2$ pulse sandwiched between XY8 decoupling sequences as a function of the microwave frequency detuning. For both $\pi/2$ pulses, we use the same maximum Rabi frequency of 12.693 MHz and for the π pulses in the XY8 sequence, we use the same maximum Rabi frequency of 26.653 MHz. For the Hermite pulse envelope, a gate with fidelity over 99.9% over a range of ±2 MHz of detuning is possible,

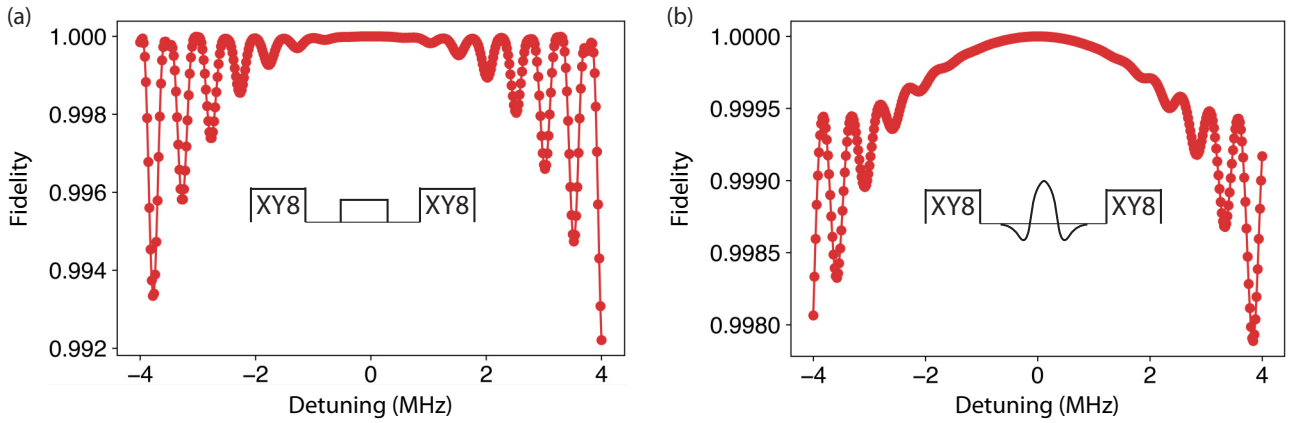

FIG. 6. Pulse fidelity of a square and Hermite $\pi/2$ pulse as a function of detuning. (a) Square $\pi/2$ pulse fidelity as a function of microwave frequency detuning. We find a rapid deterioration of pulse fidelity in the presence of detuning. We sandwich the square $\pi/2$ pulse in between XY8 decoupling sequences made of square π pulses. (b) Hermite $\pi/2$ pulse fidelity as a function of microwave frequency detuning. We obtain high pulse fidelities for a much larger range of detunings compared to the square pulse. For both the square pulse and Hermite pulse, we use a maximum Rabi frequency of 12.693 MHz for the $\pi/2$ pulse. We sandwich the Hermite $\pi/2$ pulse in between XY8 decoupling sequences made of Hermite π pulses with a maximum Rabi frequency of 26.653 MHz.

whereas for a square envelope the fidelity drops and fluctuates rapidly as a function of detuning outside the ±1 MHz range.

The nitrogen-spin gates consist of decoupling sequences on the electron spin, as described above, combined with radio-frequency pulses. Alternatively, we apply only radio-frequency pulses of approximately 100 μs in duration with the electron in $m_s = -1$ (Fig. 3). We apply the radio-frequency pulses resonant with the $m_I = 0, -1$ transition for $m_s = -1$ at a frequency of 7.120706 MHz. We add an error function envelope to each rf pulse with a risetime of 1 μs.

APPENDIX F: EFFECT OF QUASISTATIC NOISE ON XY8 DECOUPLING

In this section, we discuss the effect of quasistatic magnetic noise on the electron XY8 decoupling sequence. Such noise can originate from magnetic-field fluctuations, either from the externally applied magnetic field or from the spin bath (^{13}C nuclear spins and P1 center electron spins). For quasistatic noise, we take the magnetic field as constant for the duration of a gate. For almost all gates that we discuss, we use a decoupling sequence on the electron spin. This makes sure that any phase picked up by the electron spin due to the quasistatic bath is canceled out. Figure 7 shows a simulation of how an XY8 sequence (identity gate) responds to a constant magnetic-field detuning by extracting the average gate fidelity of the XY8 as an identity gate from the process matrix of an XY8 sequence in the electron single-qubit subspace. The simulation was conducted with the full two-qubit Hamiltonian of the system, so the gate fidelity contains information on how both the electron and nitrogen react to the quasistatic environment. From this result, we see that for a quasistatic environment, the XY8 sequence (identity gate) should ideally not show any additional infidelity.

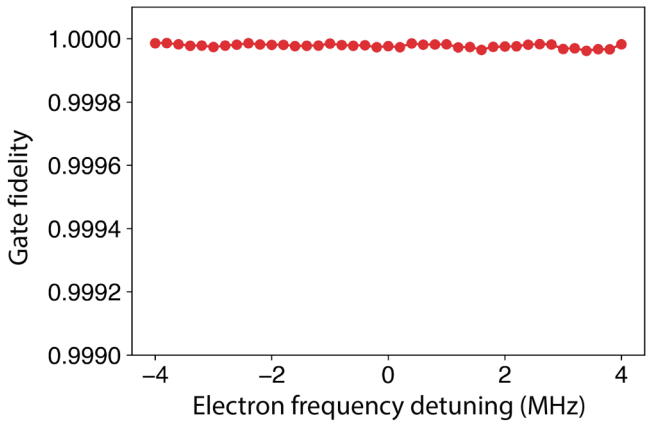

FIG. 7. Simulation of the effect of electron frequency detuning on the average gate fidelity of XY8 decoupling. We simulate the application of a single XY8 decoupling block as a function of the electron frequency detuning. We find that the effect of detuning is negligible.

APPENDIX G: NITROGEN-SPIN INITIALIZATION

In this section, we discuss the initialization of the nitrogen spin to its $m_I = 0$ state. In the gate set tomography results presented in the main text, we use SWAP-type initialization of the nitrogen spin. In Fig. 8 we show the corresponding sequence. We perform a SWAP between the electron $m_s = \{0, -1\}$ subspace and the nitrogen spin. Since the nitrogen spin is a spin-1 system, and we swap qubit-to-qubit, we need a two-step SWAP process. First, we initialize the electron spin in $m_s = 0$. Then, we perform a swap on the $m_I = \{0, -1\}$ subspace of the nitrogen spin. Next, we reinitialize the electron spin after which we perform a swap on the $m_I = \{0, +1\}$ subspace. Note that we use a reduced type of SWAP gate: as the electron spin is set to an eigenstate, the first of the three two-qubit gates can be omitted compared to the full SWAP gate of Fig. 4.

An alternative to SWAP is to use measurement-based initialization (MBI). The sequence is given in the inset of Figs. 9(a) and 9(b). First, we initialize the electron spin in $m_s = -1$, after which we apply a weak microwave pulse. This microwave flips the electron spin back to $m_s = 0$ only when the nitrogen spin is in $m_I = 0$. Finding the electron spin in $m_s = 0$ upon reading out, initializes the nitrogen spin in $m_I = 0$.

To compare the different initialization methods, we measure an electron spin resonance (ESR) spectrum after initialization of the nitrogen spin. In Fig. 9(a), we perform a single round of MBI initialization. In Fig. 9(b), we perform two rounds of MBI initialization. At the cost of a slower experimental rate, we find a significantly improved initialization fidelity. In Fig. 9(c), we show the ESR spectrum after SWAP initialization as in Fig. 8. We find a marginally improved fidelity compared to double MBI initialization.

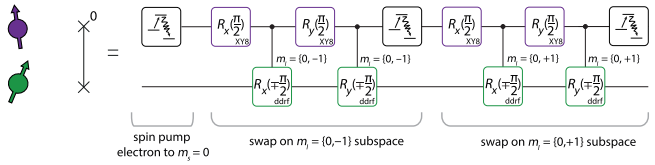

FIG. 8. Experimental sequence for SWAP initialization of the nitrogen spin. We perform a two-step SWAP process due to the spin-1 nature of the nitrogen spin. First, we perform a swap on the $m_I = \{0, -1\}$ subspace, after which we perform a swap on the $m_I = \{0, +1\}$ subspace. The gates are as defined in the main text. However, the gates on the subspace $m_I = \{0, +1\}$ of the nitrogen spin utilize a different rf frequency (Note IV within the Supplemental Material [44]). For the SWAP icon on the left, the superscript 0 indicates that this is not a full SWAP (cf. Fig. 4), but that the initialization of the electron spin in $m_s = 0$ is a requirement.

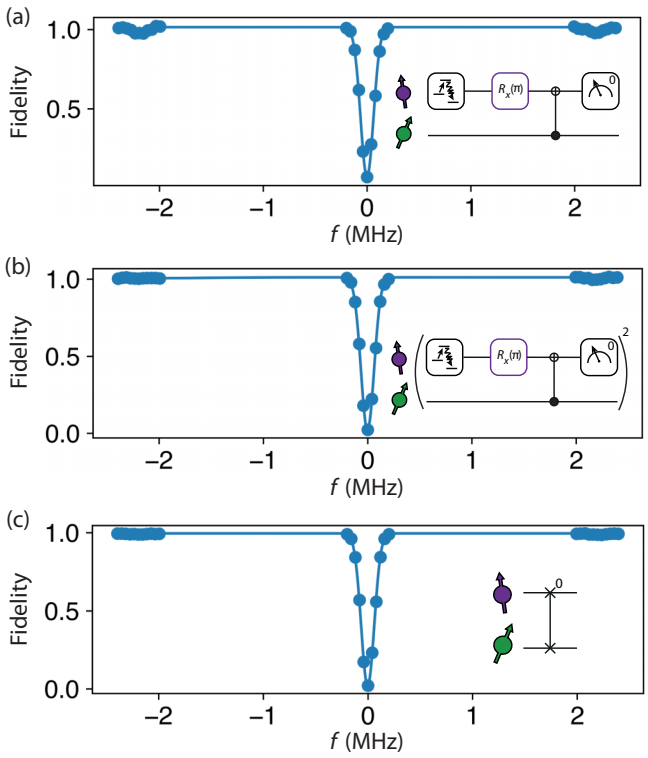

FIG. 9. ESR spectra for different initialization methods. (a) We use a single round of measurement-based initialization (MBI) to initialize the nitrogen spin. The data is fitted to the sum of three Gaussians: $a - A_1 \exp(-(x-x_1)^2/(2\sigma_1^2)) - A_2 \exp(-(x-x_2)^2/(2\sigma_2^2)) - A_3 \exp(-(x-x_3)^2/(2\sigma_3^2))$. We fit to Gaussian functions, because we used a Gaussian pulse shape to measure the ESR spectrum. We find the contrast as $A_2/(A_1 + A_2 + A_3)$ where A_2 is the amplitude of the middle dip. We find a value of 0.924(8) with a reduced chi-square of the fit of $\chi_r^2 = 1.9$. (b) We use two rounds of MBI to initialize the nitrogen spin. We find a contrast of 0.979(6) with $\chi_r^2 = 3.7$. (c) We used SWAP initialization (Fig. 8) to initialize the nitrogen spin. We find an initialization fidelity of 0.985(7) with $\chi_r^2 = 21.6$.

APPENDIX H: NITROGEN-SPIN READOUT

After each gate set tomography experiment performed in this work, we measure both the electron spin and the nitrogen spin. The full sequence to do so is given in Fig. 10. We read out the electron spin optically in a single shot [45]. Afterwards, we reinitialize the N-V electron spin in $m_s = 0$ and read out the nitrogen spin. We compile our readout out of gates characterized by GST. The applied sequence of gates maps the nitrogen z projection to the electron spin z projection, after which we read out the electron spin optically.

APPENDIX I: NITROGEN-SPIN COHERENCE

In this section, we discuss coherence measurements of the nitrogen spin. To bring the nitrogen spin in a superposition and to apply echo pulses, we use the DDRF gates

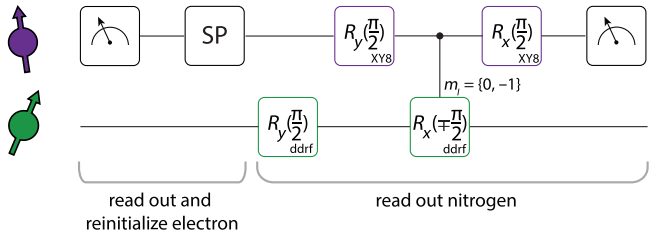

FIG. 10. Sequence to read out the electron and nitrogen spin sequentially. The electron spin is read out and initialized (by spin pump, SP) optically. The nitrogen spin is then mapped to the electron spin using only gates characterized with gate set tomography. Finally, we read out the electron spin.

(Fig. 11). First, we measure the inhomogeneous dephasing time T_2^* of the nitrogen spin for the electron spin in $m_s = 0$ [Fig. 11(a)] and $m_s = -1$ [Fig. 11(b)]. We find that T_2^* is dependent on the electron-spin state, obtaining a factor approximately 3 larger T_2^* in $m_s = 0$ compared to $m_s = -1$. We do not currently have a good explanation for this observed difference.

In Fig. 11(c) we show a nitrogen spin-echo measurement with the electron spin in $m_s = 0$. In Fig. 11(d) we show the same measurement with the electron spin in $m_s = -1$. Here, we find that the coherence time in $m_s = -1$ is longer than in $m_s = 0$, which is the opposite finding from the T_2^* measurement presented above. The observed increase in T_2 time for $m_s = -1$ may have to do with the presence of a frozen core around the N-V center, which implies that more quasistatic noise can be echoed out.

In Fig. 11(e), we show the nitrogen coherence for different numbers of echo pulses. We find an increase of coherence with increasing number of pulses, as expected. For $N = 64$, we find a coherence time of $T_2 = 73(9)$ s.

APPENDIX J: ELECTRON-SPIN COHERENCE

In this section, we discuss the electron coherence under dynamical decoupling. In Fig. 12(a), we show the electron coherence as a function of the number of π-pulses applied to the electron spin. We make sure that the interpulse delay τ is a multiple of the period set by the ^{13}C Larmor frequency to mitigate resonances from electron-nuclear interaction. While we see a steady increase in coherence time for increasing the number of pulses [Fig. 12(b)], significant outliers in the data are also visible. We attribute these to the presence of 50-Hz noise. While detrimental at large values of τ, at $\tau = 7.304$ μs, which is the value of τ used for the gate designs in this work, we are not significantly affected by this.

APPENDIX K: GATE PARAMETER CALIBRATIONS

In this section, we discuss the calibrations performed for each gate. Next to magnetic-field adjustment (Sec. D) and

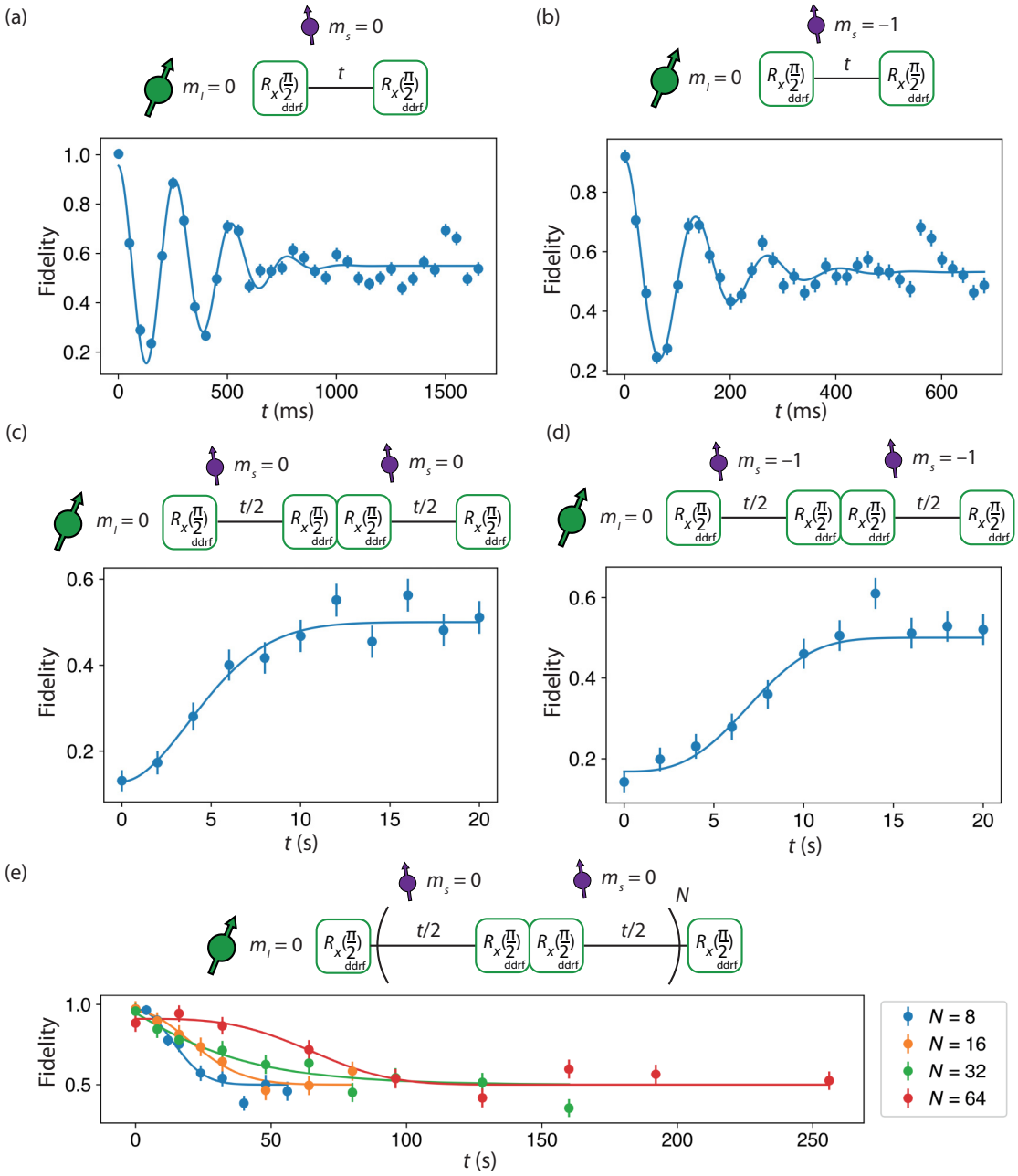

FIG. 11. Nitrogen coherence. (a) Ramsey experiment with the electron in $m_s = 0$. We find $T_2^* = 553(46)$ ms ($\chi_r^2 = 4.1$). (b) Ramsey experiment with the electron in $m_s = -1$. We find $T_2^* = 172(24)$ ms ($\chi_r^2 = 3.2$). (c) Spin-echo measurement with the electron in $m_s = 0$. We find $T_2 = 5.7(5)$ s ($\chi_r^2 = 0.97$). (d) Spin-echo measurement with the electron in $m_s = -1$. We find $T_2 = 8.0(7)$ s ($\chi_r^2 = 1.5$). (e) Nitrogen coherence for different numbers of echo pulses N. For N = 8, we find $T_2 = 18(2)$ s ($\chi_r^2 = 1.2$). For $N = 16$, we find $T_2 = 28(3)$ s ($\chi_r^2 = 0.7$). For $N = 32$, we find $T_2 = 37(10)$ s ($\chi_r^2 = 1.6$). For $N = 64$, we find $T_2 = 73(9)$ s ($\chi_r^2 = 1.2$).

balancing of the I and Q channels of the IQ modulator, we perform amplitude calibration of each single-qubit gate. The amplitude of the rf pulses for the two-qubit gate is set equal to those of the single-qubit gates and is not separately calibrated. The only difference constitutes a π-phase shift of half of the rf pulses (Fig. 2).

In Fig. 13, we show two examples of amplitude calibration. In Fig. 13(a) we apply 82 electron $\pi/2$-pulses and read out the electron spin while the nitrogen spin is in $m_I = 0$. We vary the amplitude of the $\pi/2$-pulse in the gate. The minimum is found by fitting a parabola to obtain the optimal amplitude. The π-pulses that make up the XY8

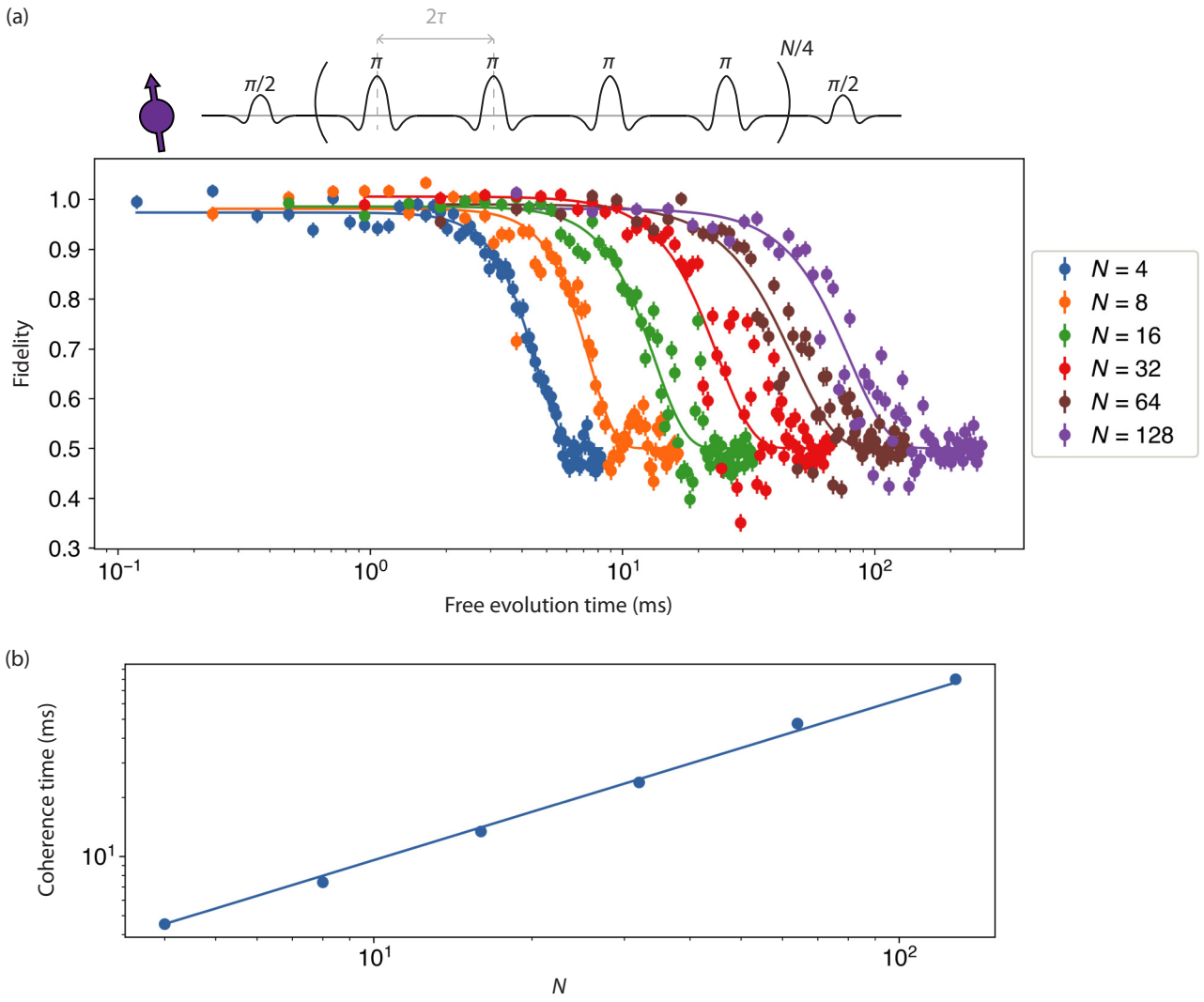

FIG. 12. Electron coherence. (a) (Top) Sequence to measure the electron coherence. We prepare the electron in a superposition and apply a number of π-pulses N. (Bottom) Experimental result. From $N = 4$ to $N = 128$ we find, respectively, $T_2 = 4.53(4)$ ms ($\chi_r^2 = 1.9$), $T_2 = 7.4(2)$ ms ($\chi_r^2 = 7.5$), $T_2 = 13.4(4)$ ms ($\chi_r^2 = 9.5$), $T_2 = 23.9(9)$ ms ($\chi_r^2 = 17.7$), $T_2 = 48(2)$ ms ($\chi_r^2 = 9.3$), $T_2 = 80(3)$ ms ($\chi_r^2 = 7.7$). (b) Scaling of the coherence time with the number of pulses N. We fit to $T_{N=4}(N/4)^\eta$ where $T_{N=4}$ is the coherence time for $N = 4$. We find $\eta = 0.82(2)$ ($\chi_r^2 = 27.3$).

sequence are calibrated similarly. In Fig. 13(b) we apply 98 nitrogen $\pi/2$-pulses with DDRF and read out the nitrogen spin. We vary the amplitude of the rf driving of the nitrogen spin. The maximum value of the fit gives the optimal amplitude for the rf driving.

APPENDIX L: SINGLE-SHOT READOUT CORRECTION

For the results shown in Figs. 2 and 4 of the main text as well as in many figures (Figs. 5, 9, 11, 12, 13, 15, 16, 18, 19, 20, 21), we correct the electron measurement results for known readout errors. We do this by using single-shot readout (SSRO) correction following Pompili *et al.* [3]. Before and during our measurements, we run SSRO calibrations to find $F_0 = P(\text{measure} m_s = 0 | \text{state is } m_s = 0)$ and similarly F_1. Now the measurement of the electron spin can be described by

$$\mathbf{m} = \begin{pmatrix} F_0 & 1 - F_1 \\ 1 - F_0 & F_1 \end{pmatrix} \mathbf{p}. \tag{L1}$$

Here, $\mathbf{m} = (m_0\ m_1)^{\mathrm{T}}$ is a vector with measured populations and $\mathbf{p} = (p_0\ p_1)^{\mathrm{T}}$ is a vector with the true populations we expect based on the measurement fidelities. Measuring m_0, m_1, F_0, and F_1, we obtain p_0 and p_1 by matrix inversion. For example, for 500 repetitions of preparing the electron spin in $m_s = 0$ and reading it out, one could measure 406 occurrences of $m_s = 0$. This gives $m_0 = 406/500$ and $m_1 = 94/500$. Using typical values of $F_0 = 82\%$ and

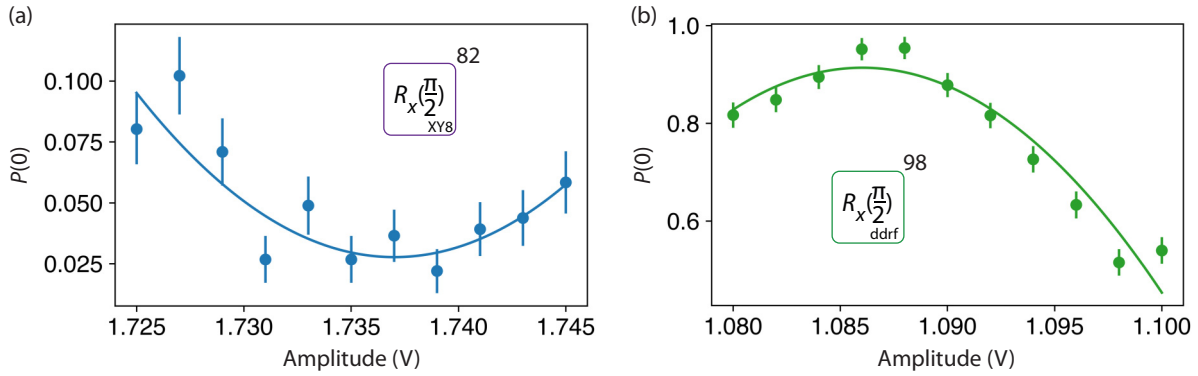

FIG. 13. Amplitude calibration of electron and nitrogen gates. (a) We apply 82 electron $\pi/2$ gates while sweeping the amplitude of the $\pi/2$-pulse. By fitting to $A + a(x - x_0)^2$, we obtain the optimal amplitude of 1.7370(9) V ($\chi_r^2 = 1.4$). (b) We apply 98 nitrogen $\pi/2$ gates while sweeping the rf amplitude in the DDRF gate. We find the optimal amplitude at 1.0860(9) V ($\chi_r^2 = 3.6$). The y-axis label $P(0)$ represents the probability to measure the 0 state of the electron (a) or nitrogen (b) spin state.

$F_1 = 99\%$ this gives $p_0 = 0.99$ and $p_1 = 1 - p_0 = 0.01$. Note that this method can return nonphysical central values due to noise (e.g., a population number exceeding one). An alternative method to do SSRO correction is iterative Bayesian unfolding [88].

For readout of the nitrogen spin, its state is mapped to the electron spin and subsequently measured as an electron-spin state (see Appendix H). Therefore, we also use the correction described in this section for measurements of the nitrogen spin state. Note that we do not correct for the infidelity of the readout circuit of the nitrogen spin, which explains why the fidelities are typically not perfect (see, e.g., Fig. 11).

The error bars on the data in the relevant figures (Figs. 2, 4, 5, 9, 11, 12, 13, 15, 16, 18, 19, 20, 21) represent one standard deviation and are calculated using the measured populations m_0, m_1. The uncertainty on m_0, m_1 is binomial:

$$\sigma_{m_0} = \sigma_{m_1} = \sqrt{\frac{m_0(1 - m_0)}{N}}, \tag{L2}$$

where N is the number of experimental repetitions. We can invert Eq. (L1) to obtain the error on the expected populations [3]:

$$\sigma_{p_0} = \sigma_{p_1} = \frac{\sigma_{m_0}}{F_0 + F_1 - 1}. \tag{L3}$$

APPENDIX M: RANDOMIZED BENCHMARKING

A common method to characterize quantum gates is randomized benchmarking (RB) [51–56]. Randomized benchmarking gives a metric for how well a quantum state "survives" sequences of random quantum gates. In contrast to the GST that we use in the main text, randomized benchmarking does not provide the full process matrix. Here, we perform (single-qubit) Clifford RB and compare against the results obtained from single-qubit GST. The protocol is as follows (see also the illustration in Fig. 14):

(1) Random sequences of Clifford gates of different depths (lengths) are generated.

(2) An inversion gate (also a Clifford gate) is calculated and appended to the random sequence. For half of the sequences, the inversion gate theoretically makes the total sequence equal to identity. For the other half, the inversion gate additionally incorporates a π-pulse, rotating the measurement basis.

(3) The Clifford gates are compiled out of native gates [identity, $X(\pi/2)$, $Y(\pi/2)$]. The native gates were chosen to be the same as the gates characterized with GST. The average number of native gates per Clifford gate is $N = 3.125$.

(4) The compiled sequences are run on either the initialized electron spin (500 repetitions) or the initialized nuclear spin (1000 repetitions). The obtained counts are corrected for electron readout fidelity (Sec. L).

(5) We plot the survival probability P of the quantum state as a function of native gate sequence depth m. We fit $P = A + Bp^m$ to the average survival probabilities per depth, taking the binomial uncertainties on the points (see Sec. L) as relative weights. We extract the depolarizing parameter p. A and B are values that capture the state preparation and measurement errors. A is fixed to 0.5.

(6) The average gate infidelity r is calculated using $r = \frac{(2^n-1)(1-p)}{2^n}$ where n is the number of qubits. The average gate fidelity is $F_{\text{avg}} = 1 - r$.

To be able to compare the results from RB and GST, we use a simulation to generate RB data based on the process matrices of the native gates, that were obtained using GST [47]. The simulated RB data is analyzed in a similar fashion as the experimental RB data. Then, the average gate fidelities of both methods can be compared. GST gives gate fidelities for the native gates separately. As a sanity check, we took the average of these gate fidelities, weighted by their occurrence in the RB sequences

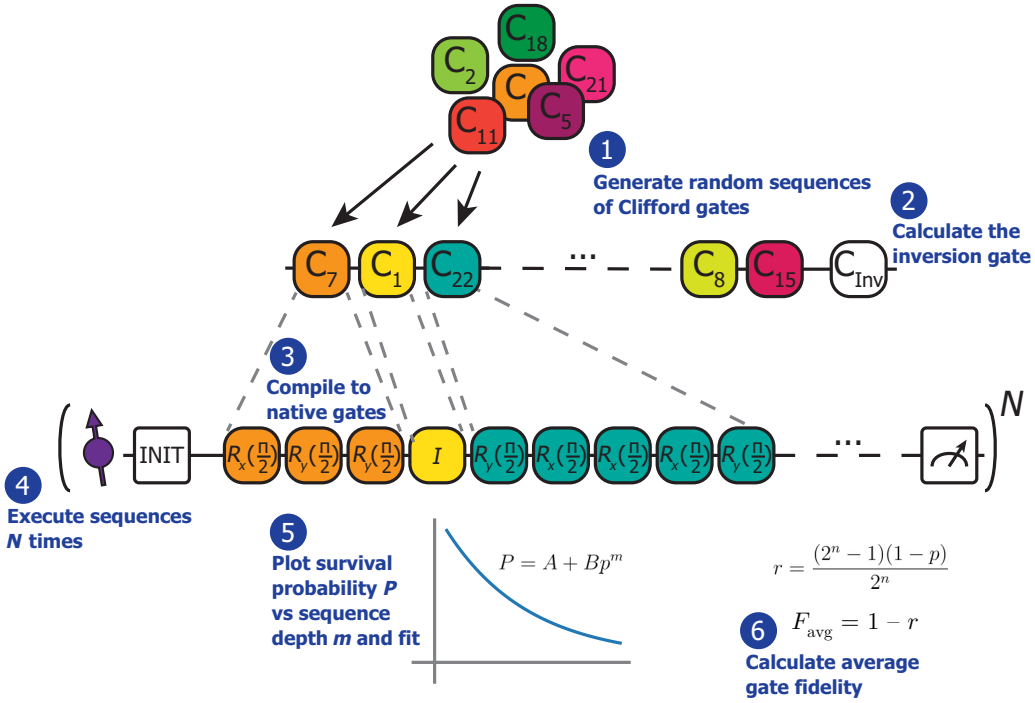

FIG. 14. Illustration of the Clifford randomized benchmarking protocol.

used for both experiment and simulation, and compared the weighted average to the RB simulation. In all three cases described below, this weighted average was—within error—the same as the result of the RB simulation. This indicates that one can directly compare the weighted average gate fidelity of the GST report to an average gate fidelity found with RB.

1. RB on the electron spin

We generate 30 random sequences of Clifford gates for each depth $m_C \in \{5, 10, 20, 50, 100, 200, 500, 750\}$ Clifford gates. The inversion gate (also a Clifford gate) theoretically returns the quantum state to the measurement basis, which we alternate between the electron state $m_s = 0$ and $m_s = -1$.

Figure 15(a) shows the survival probability for each sequence. For this experiment, the nitrogen spin was initialised in $m_I = 0$. The identity gate consists of an XY8 decoupling sequence [Fig. 2(a)]. The $\pi/2$ gates around x and y are Hermite pulses without XY8 decoupling sequences around them [Fig. 3(a)]. We find a depolarizing parameter $p = 0.99991(1)$ ($\chi_r^2 = 40.7$). The average gate fidelity of a native gate is $F_{\text{avg}} = 0.999956(6)$.

With GST, we also investigated this experimental regime with the nitrogen initialized in $m_I = 0$ and no decoupling sequences around the $\pi/2$ gates. The results are shown on the right-hand side of Fig. 3(b). With the process matrices obtained from this GST characterization, we simulate RB data (with a binomial spread) using the pygsti package [82]. For this, the same random sequences are used as for the actual RB experiment. The results are shown in Fig. 15(b). We found a depolarizing parameter $p = 0.999717(4)$ ($\chi_r^2 = 1.30$), resulting in an average gate fidelity of $F_{\text{avg}} = 0.999859(2)$. This is in correspondence with the weighted (for their occurrence in the RB sequences) average of the gate fidelities from GST, which is 0.99985(3).

Interestingly, the average gate fidelity found with experimental RB ($F_{\text{avg}} = 0.999956(6)$) is significantly higher than the average gate fidelity reported by the experimental GST ($F = 0.99985(3)$). This can be an indication of non-Markovianity in our system, for example in the form of slow fluctuations of the magnetic field. This type of error manifests as a coherent error that is the same within one measurement repetition, but differs from repetition to repetition. Since GST amplifies coherent errors, it is relatively sensitive to such low-frequency noise, whereas the random nature of RB sequences makes it relatively insensitive [47]. The large spread in survival probabilities for the actual RB experiment (especially for long sequences) may also be related to the non-Markovianity in our system. The large χ_r^2 can also be an indication of the noise being non-Markovian [53,89].

The results in Fig. 16 are from a similar experiment. Except here, there are XY8 sequences around the $\pi/2$-pulses around x and y [Fig. 2(a)]. The nitrogen was initialized in $m_I = 0$. From the fit, we obtain a depolarizing parameter $p = 0.99941(2)$ ($\chi_r^2 = 11.6$). The average gate fidelity of a native gate is $F_{\text{avg}} = 0.99970(1)$. Figure 16(b)

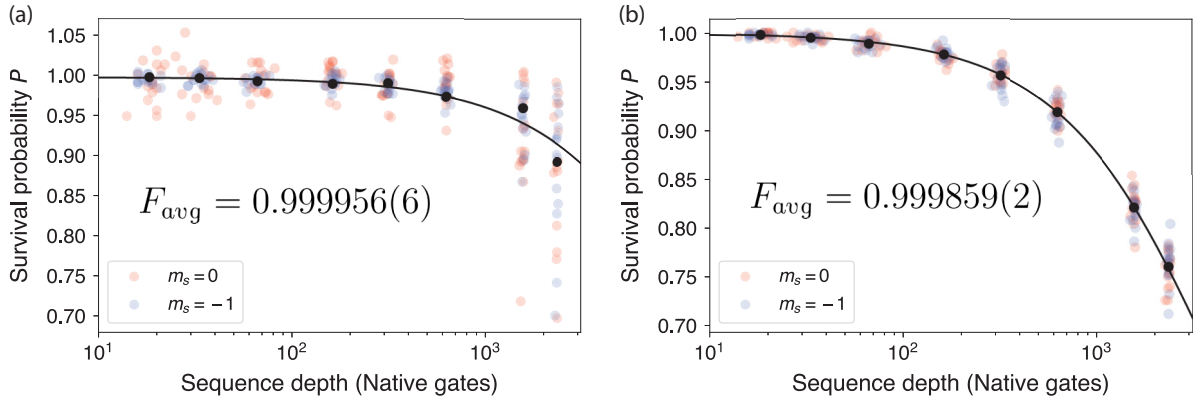

FIG. 15. Electron RB results. The nitrogen spin is initialized in $m_I = 0$ and no decoupling sequences are used around the $\pi/2$ gates. Red (blue) dots are values resulting from a sequence ending with an inversion gate bringing the spin to $m_s = 0$ ($m_s = -1$). Black dots are the average of all survival probabilities belonging to one Clifford depth $m_C \in \{5, 10, 20, 50, 100, 200, 500, 750\}$. The black line is a fit to the black dots. Error bars on the black dots are binomial errors and smaller than the data points. (a) Experimental result. The depolarizing parameter is $p = 0.99991(1)$ ($\chi_r^2 = 40.7$), resulting in an average gate fidelity of $F_{\text{avg}} = 0.999956(6)$. (b) Simulation of the RB experiment based on the process matrices obtained with GST. The depolarizing parameter $p = 0.999717(4)$ ($\chi_r^2 = 1.30$) results in an average gate fidelity of $F_{\text{avg}} = 0.999859(2)$.

shows simulated data based on the process matrices of the gates, that were obtained by the GST experiment reported in Fig. S3b, second column. We find a depolarizing parameter $p = 0.999578(8)$ ($\chi_r^2 = 2.42$). The average gate fidelity of a native gate is $F_{\text{avg}} = 0.999789(4)$. This value is the same as the weighted average of the gate fidelities of the GST report, which is 0.99979(5).

Again, there is a discrepancy between the average gate fidelity found with RB and the average gate fidelity found with GST. However, it is significantly smaller, possibly because the XY8 decoupling sequences around the Hermite pulses reduce the non-Markovianity in our system.

Figure 17(a) shows the results of another RB experiment with XY8 sequences around the $\pi/2$-pulses. Here, we use a decoupling time τ of 2.0 μs. We find a depolarizing parameter $p = 0.99957(1)$ ($\chi_r^2 = 6.56$), resulting in an average gate fidelity of $F_{\text{avg}} = 0.999783(7)$. Figure 17(b) shows simulated data based on the process matrices of the gates, that were obtained by doing the GST experiment of which the results are shown in Fig. S3b, third

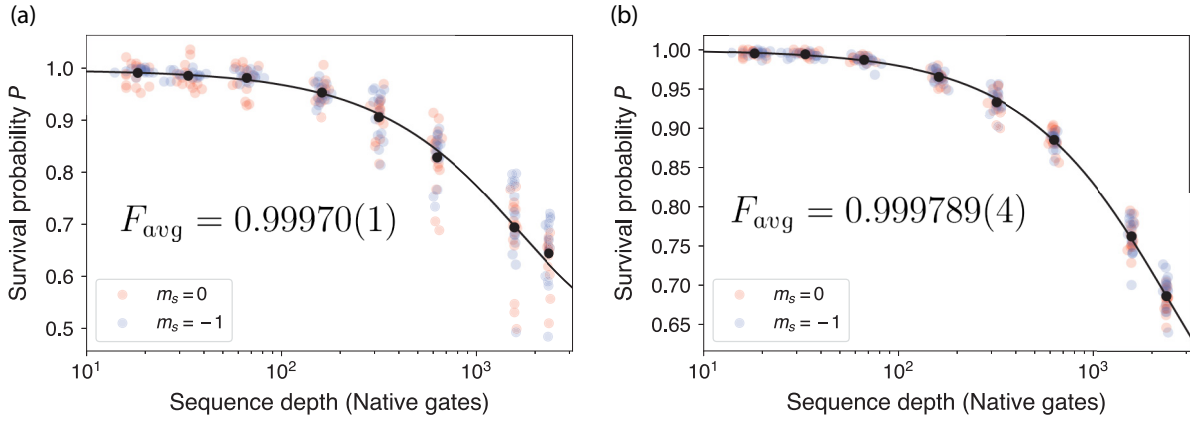

FIG. 16. Electron RB results. The nitrogen spin is initialized in $m_I = 0$ and there are XY8 decoupling sequences around the $\pi/2$ gates. Red (blue) dots are values resulting from a sequence ending with an inversion gate bringing the spin to $m_s = 0$ ($m_s = -1$). Black dots are the average of all survival probabilities belonging to one Clifford depth $m_C \in \{5, 10, 20, 50, 100, 200, 500, 750\}$. Black line is a fit to the black dots. Error bars on the black dots are binomial errors and smaller than the data points. (a) Experimental results. The depolarizing parameter is $p = 0.99941(2)$ ($\chi_r^2 = 11.6$), resulting in an average gate fidelity of $F_{\text{avg}} = 0.99970(1)$. (b) Simulation of RB experiment based on the process matrices obtained with GST. The depolarizing parameter $p = 0.999578(8)$ ($\chi_r^2 = 2.42$) results in an average gate fidelity of $F_{\text{avg}} = 0.999789(4)$.

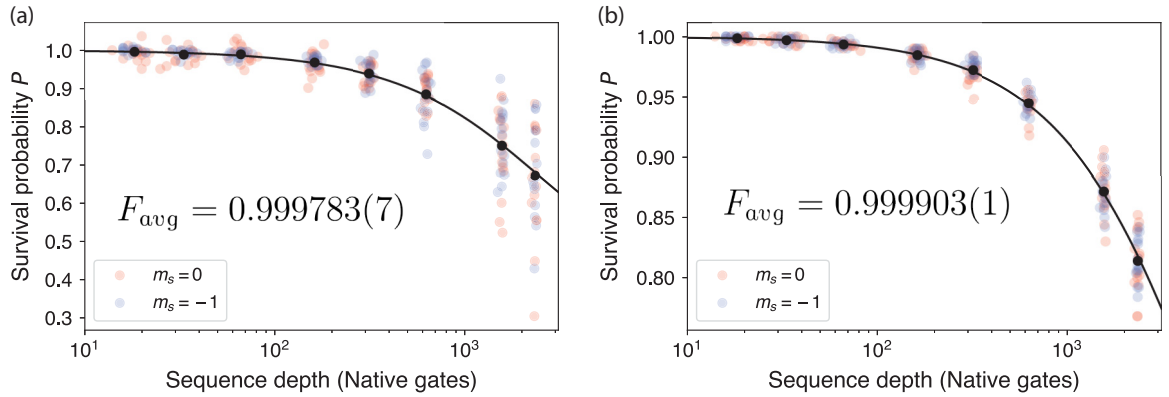

FIG. 17. Electron RB results. The nitrogen spin is initialized in $m_I = 0$ and there are XY8 decoupling sequences around the $\pi/2$ gates, with $\tau = 2.0$ μs. Red (blue) dots are values resulting from a sequence ending with an inversion gate bringing the spin to $m_s = 0$ ($m_s = -1$). Black dots are the average of all survival probabilities belonging to one Clifford depth $m_C \in \{5, 10, 20, 50, 100, 200, 500, 750\}$. Black line is a fit to the black dots. Error bars on the black dots are binomial errors and smaller than the data points. (a) Experimental results. The depolarizing parameter is $p = 0.99957(1)$ ($\chi_r^2 = 6.56$), resulting in an average gate fidelity of $F_{\mathrm{avg}} = 0.999783(7)$. (b) Simulation of RB experiment based on the process matrices obtained with GST. The depolarizing parameter $p = 0.999807(3)$ ($\chi_r^2 = 0.81$) results in an average gate fidelity of $F_{\mathrm{avg}} = 0.999903(1)$.

column. The simulation gives a depolarizing parameter $p = 0.999807(3)$ ($\chi_r^2 = 0.81$) and an average gate fidelity of $F_{\mathrm{avg}} = 0.999903(1)$. This value is the same as the weighted average of the gate fidelities of the GST report, which is 0.99990(4).

2. RB on the nitrogen spin

The results for RB on the nitrogen spin are shown in Fig. 18(a). Here, the electron is in an eigenstate ($m_s = 0$) and we use DDRF gates [Fig. 2(a)]. As expected, there is no visible decay for these depths. This data should be compared to the GST results shown on the right-hand side of Fig. 3(c). Using the process matrices obtained with that GST experiment, we simulate the RB experiment in Fig. 18(b). We find $p = 0.999937(6)$ ($\chi_r^2 = 3.12$). The average gate fidelity of a native gate is 0.999968(3). The weighted average of the gate fidelities from the GST report is 0.99996(3).

APPENDIX N: SWAP: COMPARISON TO THE GST PREDICTION

In Fig. 4(b) of the main text, we apply the compiled SWAP gate n times. After an even number of SWAPs, we then measure the average state fidelity of the six cardinal

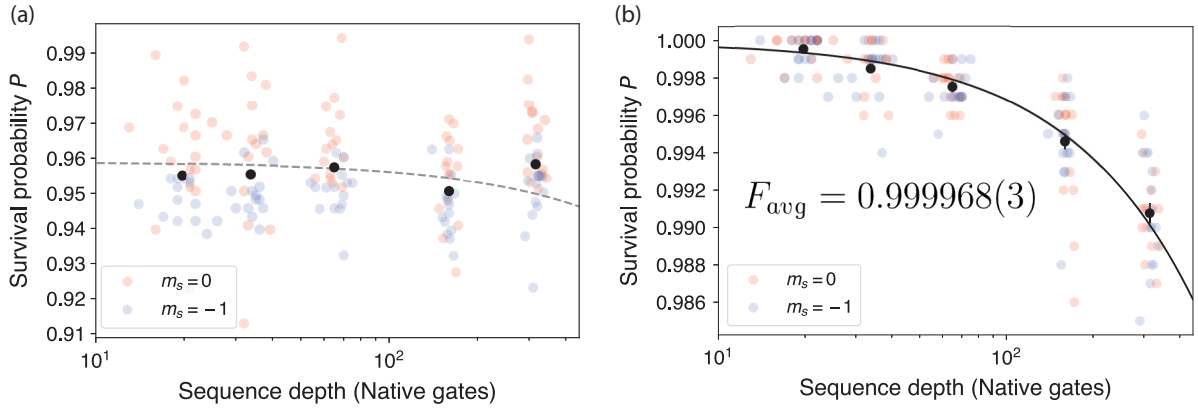

FIG. 18. Nitrogen RB results. The electron was initialized in $m_s = 0$ and DDRF gates were used [Fig. 2(a)]. Red (blue) dots are values resulting from a sequence ending with an inversion gate bringing the nitrogen spin to the state that is mapped to $m_s = 0$ ($m_s = -1$) during readout. Black dots are the average of all survival probabilities belonging to one Clifford depth $m_C \in \{5, 10, 20, 50, 100\}$. (a) Experimental result. The RB experiment took ∼3 h compared to approximately 1.5 h for the GST results in Fig. 3(c), right-hand side. There is no decay that could be fit. The dotted line is an exponential decay with the decay parameter obtained from the simulation in (b), for comparison. (b) Simulation of RB experiment based on the process matrices obtained with GST. Black line is a fit to the black dots, yielding a depolarizing parameter of $p = 0.999937(6)$ ($\chi_r^2 = 3.12$). This gives an average gate fidelity of $F_{\mathrm{avg}} = 0.999968(3)$.

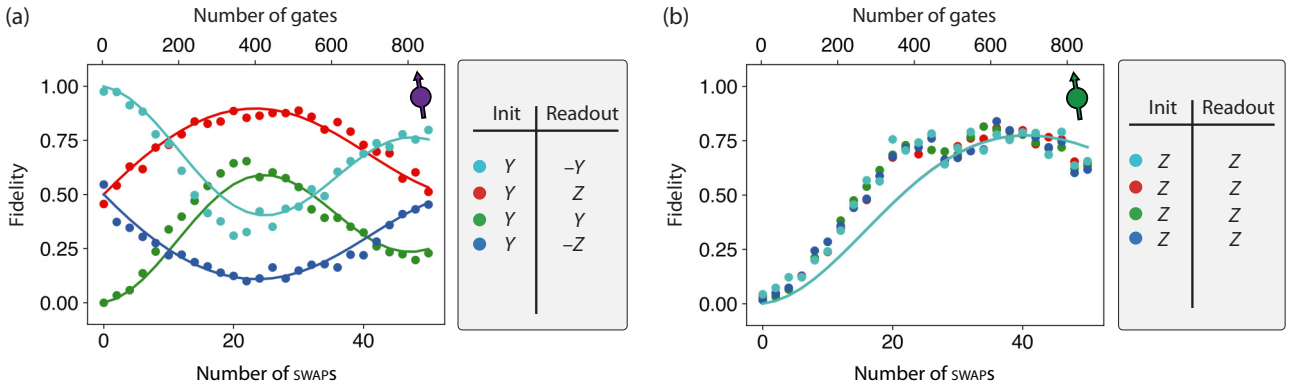

FIG. 19. Comparison of GST-based prediction to experiment for different spin components. (a) Electron-spin population measured along different cardinal axes (points) and corresponding GST predictions (lines). (b) Nitrogen spin population measured along z (points) and corresponding GST predictions (lines). The error bars are smaller than the data points.

states:

$$F_{\text{avg}} = \frac{1}{6}\sum_{i=1}^{6} \langle\psi|_i \, \rho_i \, |\psi\rangle_i \,, \tag{N1}$$

with $|\psi\rangle_i \in \{|Z\rangle, |-Z\rangle, |X\rangle, |-X\rangle, |Y\rangle, |-Y\rangle\}$, and with ρ_i the experimentally obtained state (ideally $\rho_i = |\psi\rangle_i \langle\psi|_i$).

For this purpose, the electron is initialized to each of the cardinal axes and the nitrogen is initialized in $m_I = 0$. At the end of an even number of SWAP gates, we measure the projections of the electron spin onto all cardinal axes, and the nitrogen spin along z.

The average state fidelity after n SWAP gates is well reproduced by the process matrices obtained from two-qubit GST. Moreover, the action of the full gate sequence on the individual spin components of both electron and nitrogen spin can be reproduced. This is illustrated in Fig. 19, which shows an example of state preparation and measurement in different bases and its comparison to the GST prediction. The results corroborate the accuracy of the process matrices obtained from GST.

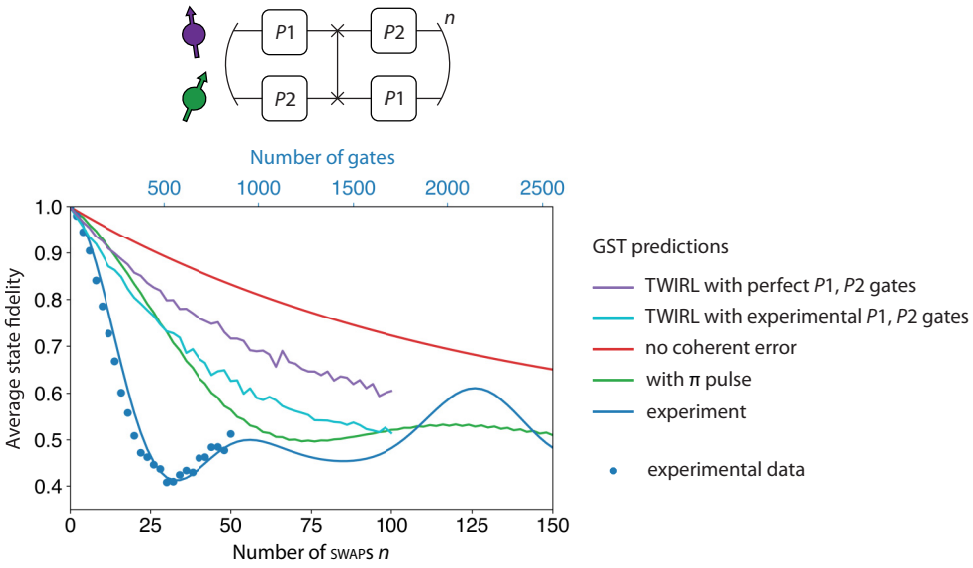

FIG. 20. Theoretical analysis of error mitigation techniques on the electron-nitrogen SWAP gate sequence. Similar to Fig. 4(b) of the main text, with the addition of Pauli twirling to mitigate the build-up of coherent errors. Top: Pauli-twirling compilation for the SWAP gate. For each realization and each SWAP we choose P_1 and P_2 at random. For perfect Pauli operations, this block is identical to a simple SWAP. Bottom: comparison of different mitigation techniques for the n sequential SWAP gate sequence. Both electron π-pulse echo (green) and Pauli twirling with experimental gates for P_1, P_2 (light blue, experimental gates as characterized in Fig. 2) or perfect gates for P_1, P_2 (purple) are simulated to improve the average state fidelity. The error bars are smaller than the data points.

Even though the average state fidelity after $n = 20$ SWAP operations reaches 0.5, the individual electron spin components clearly show coherent rotations well beyond that, which are expected to come from coherent errors. Together with the predictive power of GST, this can be used to design tailored error mitigation to cancel the effect of accumulated coherent errors in specific extended gate sequences (Sec. O).

APPENDIX O: SWAP: ERROR-MITIGATION TECHNIQUES

As illustrated in Fig. 4(b) of the main text, the average fidelity of the six cardinal electron states after an even number of SWAPs is mainly limited by an accumulation of coherent errors. The particular sequence is close to a worst-case scenario, as the same gate is repeated n times, allowing coherent errors to add up with circuit depth. As circuits of practical interest are in general not random, the effect of coherent errors on the results will likely be significant. The direct solution is to improve the precision of the calibration of the basic gate parameters in order to further reduce the coherent errors. However, this can be challenging at the high-fidelity levels achieved here.

We highlight two different solutions to this issue using GST process matrix simulations, the results of which are illustrated in Fig. 20. First, using GST, we can determine the accumulated coherent error of a particular larger circuit block. In principle, this could allow one to tailor a specific gate sequence that cancels the effect of the coherent error completely. In the particular sequence at hand, a significant portion of the coherent error is due to a $Z_e I_n$ error during the controlled two-qubit gate. Therefore, echo pulses on the electron after each swap (compiled as two electron $X_{\pi/2}$ gates), can significantly decrease the accumulated coherent error (Fig. 20).

Second, we can use error-mitigation techniques such as Pauli twirling, which was recently also used in the context of error extrapolation [90–93]. Due to the twirling, the coherent errors cannot add up linearly. In our case, we can build a Pauli-twirling set from our characterized gates as $\{I, X_{\pi/2} * X_{\pi/2}, Y_{\pi/2} * Y_{\pi/2}, X_{\pi/2} * Y_{\pi/2} * X_{\pi/2} * Y_{\pi/2}\}$. The twirling operations are compiled as illustrated in Fig. 20. For the simulation, we average over ten different realizations, picking a Pauli P_1 and P_2 randomly from the twirling set for each SWAP in the sequence. As we can see in the figure, the Pauli twirling does not allow for a coherent accumulation of errors, resulting in an exponential decay of the average fidelity of the six cardinal states. Comparing to ideal Pauli gates, we note that the effectiveness of this error mitigation technique relies on high-fidelity single-qubit gates. These theoretical simulations for the example case (repeated SWAPs) illustrate that the GST characterisation can be used to determine tailored error mitigation methods to improve the fidelity of circuit blocks.

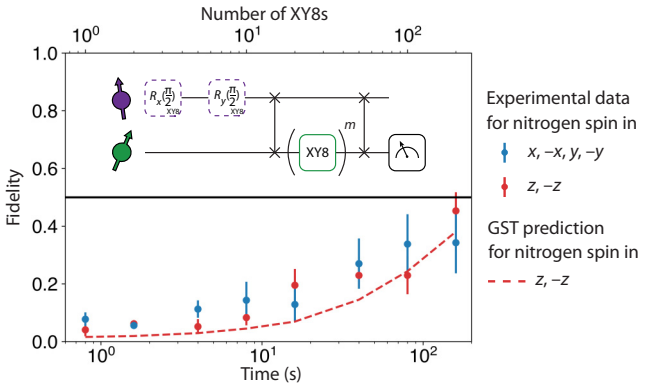

FIG. 21. Electron-spin population during nitrogen decoupling. After storing a quantum state ($\pm x$, $\pm y$, or $\pm z$) on the nitrogen spin and swapping it back to the electron spin, we measure the nitrogen spin to determine what happened to the electron spin during the decoupling sequence on the nitrogen spin. The electron-spin population decays for increasing numbers of XY8s. The timescale is similar to the decoherence of the nitrogen spin in Fig. 4(c), suggesting that control errors in the DDRF $\pi/2$ gates used to construct the nitrogen spin XY8 decoupling sequence lead to the observed decay.

APPENDIX P: QUANTUM MEMORY: ELECTRON-SPIN DEPOLARIZATION DURING NITROGEN-SPIN DECOUPLING

In this section, we discuss additional data accompanying Fig. 4(c). In Fig. 4(c), we read out the electron spin, which gives information about the state that was stored on the nitrogen spin during the main evolution time. In Fig. 21, we read out the nitrogen spin, which gives information about what happened to the electron spin during the decoupling sequence on the nitrogen spin. We find that the electron spin population decays during XY8 decoupling of the nitrogen spin. A similar decay is predicted from the two-qubit GST process matrices, even though we did not include electron-spin dephasing during the free-evolution time in this prediction, as this depends on the detailed, microscopic spin-bath dynamics. The electron-spin depolarization occurs at the same timescale as the nitrogen spin decoherence in Fig. 4(c), which suggests that electron-spin control errors in the DDRF gate are the underlying cause of the observed nitrogen spin decoherence, instead of direct decoherence of the nitrogen spin due to the surrounding spin bath.

[1] D. D. Awschalom, R. Hanson, J. Wrachtrup, and B. B. Zhou, Quantum technologies with optically interfaced solid-state spins, Nat. Photonics **12**, 516 (2018).

[2] B. Hensen, H. Bernien, A. E. Dréau, A. Reiserer, N. Kalb, M. S. Blok, J. Ruitenberg, R. F. L. Vermeulen, R. N. Schouten, C. Abellán, W. Amaya, V. Pruneri, M. W. Mitchell, M. Markham, D. J. Twitchen, D. Elkouss, S. Wehner, T. H. Taminiau, and R. Hanson, Loophole-free Bell inequality violation using electron spins separated by 1.3 kilometres, Nature **526**, 682 (2015).

[3] M. Pompili, S. L. N. Hermans, S. Baier, H. K. C. Beukers, P. C. Humphreys, R. N. Schouten, R. F. L. Vermeulen, M. J. Tiggelman, L. dos Santos Martins, B. Dirkse, S. Wehner, and R. Hanson, Realization of a multinode quantum network of remote solid-state qubits, Science **372**, 259 (2021).

[4] S. L. N. Hermans, M. Pompili, H. K. C. Beukers, S. Baier, J. Borregaard, and R. Hanson, Qubit teleportation between non-neighbouring nodes in a quantum network, Nature **605**, 663 (2022).

[5] C. M. Knaut, A. Suleymanzade, Y.-C. Wei, D. R. Assumpcao, P.-J. Stas, Y. Q. Huan, B. Machielse, E. N. Knall, M. Sutula, G. Baranes, N. Sinclair, C. De-Eknamkul, D. S. Levonian, M. K. Bhaskar, H. Park, M. Lončar, and M. D. Lukin, Entanglement of nanophotonic quantum memory nodes in a telecom network, Nature **629**, 573 (2024).

[6] C. E. Bradley, J. Randall, M. H. Abobeih, R. C. Berrevoets, M. J. Degen, M. A. Bakker, M. Markham, D. J. Twitchen, and T. H. Taminiau, A ten-qubit solid-state spin register with quantum memory up to one minute, Phys. Rev. X **9**, 031045 (2019).

[7] C. T. Nguyen, D. D. Sukachev, M. K. Bhaskar, B. Machielse, D. S. Levonian, E. N. Knall, P. Stroganov, R. Riedinger, H. Park, M. Lončar, and M. D. Lukin, Quantum network nodes based on diamond qubits with an efficient nanophotonic interface, Phys. Rev. Lett. **123**, 183602 (2019).

[8] A. Bourassa, C. P. Anderson, K. C. Miao, M. Onizhuk, H. Ma, A. L. Crook, H. Abe, J. Ul-Hassan, T. Ohshima, N. T. Son, G. Galli, and D. D. Awschalom, Entanglement and control of single nuclear spins in isotopically engineered silicon carbide, Nat. Mater. **19**, 1319 (2020).

[9] J. Randall, C. E. Bradley, F. V. van der Gronden, A. Galicia, M. H. Abobeih, M. Markham, D. J. Twitchen, F. Machado, N. Y. Yao, and T. H. Taminiau, Many-body-localized discrete time crystal with a programmable spin-based quantum simulator, Science **374**, 1474 (2021).

[10] V. Vorobyov, S. Zaiser, N. Abt, J. Meinel, D. Dasari, P. Neumann, and J. Wrachtrup, Quantum Fourier transform for nanoscale quantum sensing, npj Quantum Inf. **7**, 124 (2021).

[11] S. B. van Dam, J. Cramer, T. H. Taminiau, and R. Hanson, Multipartite entanglement generation and contextuality tests using nondestructive three-qubit parity measurements, Phys. Rev. Lett. **123**, 050401 (2019).

[12] T. van der Sar, Z. H. Wang, M. S. Blok, H. Bernien, T. H. Taminiau, D. M. Toyli, D. A. Lidar, D. D. Awschalom, R. Hanson, and V. V. Dobrovitski, Decoherence-protected quantum gates for a hybrid solid-state spin register, Nature **484**, 82 (2012).

[13] Y. Wang, F. Dolde, J. Biamonte, R. Babbush, V. Bergholm, S. Yang, I. Jakobi, P. Neumann, A. Aspuru-Guzik, J. D. Whitfield, and J. Wrachtrup, Quantum simulation of helium hydride cation in a solid-state spin register, ACS Nano **9**, 7769 (2015).

[14] J. Zhang, S. S. Hegde, and D. Suter, Efficient implementation of a quantum algorithm in a single nitrogen-vacancy center of diamond, Phys. Rev. Lett. **125**, 030501 (2020).

[15] J. Cramer, N. Kalb, M. A. Rol, B. Hensen, M. S. Blok, M. Markham, D. J. Twitchen, R. Hanson, and T. H. Taminiau, Repeated quantum error correction on a continuously encoded qubit by real-time feedback, Nat. Commun. **7**, 1 (2016).

[16] G. Waldherr, Y. Wang, S. Zaiser, M. Jamali, T. Schulte-Herbrüggen, H. Abe, T. Ohshima, J. Isoya, J. F. Du, P. Neumann, and J. Wrachtrup, Quantum error correction in a solid-state hybrid spin register, Nature **506**, 204 (2014).

[17] M. H. Abobeih, Y. Wang, J. Randall, S. J. H. Loenen, C. E. Bradley, M. Markham, D. J. Twitchen, B. M. Terhal, and T. H. Taminiau, Fault-tolerant operation of a logical qubit in a diamond quantum processor, Nature **606**, 884 (2022).

[18] E. Knill, Quantum computing with realistically noisy devices, Nature **434**, 39 (2005).

[19] P. Aliferis, D. Gottesman, and J. Preskill, Quantum accuracy threshold for concatenated distance-3 codes, Quantum Inf. Comput. **6**, 97 (2006).

[20] B. M. Terhal, Quantum error correction for quantum memories, Rev. Mod. Phys. **87**, 307 (2015).

[21] S. de Bone, P. Möller, C. E. Bradley, T. H. Taminiau, and D. Elkouss, Thresholds for the distributed surface code in the presence of memory decoherence, AVS Quantum Sci. **6**, 033801 (2024).

[22] X. Rong, J. Geng, F. Shi, Y. Liu, K. Xu, W. Ma, F. Kong, Z. Jiang, Y. Wu, and J. Du, Experimental fault-tolerant universal quantum gates with solid-state spins under ambient conditions, Nat. Commun. **6**, 8748 (2015).

[23] H. H. Vallabhapurapu, I. Hansen, C. Adambukulam, R. Stöhr, A. Denisenko, C. H. Yang, and A. Laucht, High-fidelity control of a nitrogen-vacancy-center spin qubit at room temperature using the sinusoidally modulated, always rotating, and tailored protocol, Phys. Rev. A **108**, 022606 (2023).

[24] T. Xie, Z. Zhao, S. Xu, X. Kong, Z. Yang, M. Wang, Y. Wang, F. Shi, and J. Du, 99.92%-fidelity cnot gates in solids by noise filtering, Phys. Rev. Lett. **130**, 030601 (2023).

[25] W. Huang, C. H. Yang, K. W. Chan, T. Tanttu, B. Hensen, R. C. C. Leon, M. A. Fogarty, J. C. C. Hwang, F. E. Hudson, K. M. Itoh, A. Morello, A. Laucht, and A. S. Dzurak, Fidelity benchmarks for two-qubit gates in silicon, Nature **569**, 532 (2019).

[26] A. R. Mills, C. R. Guinn, M. J. Gullans, A. J. Sigillito, M. M. Feldman, E. Nielsen, and J. R. Petta, Two-qubit silicon quantum processor with operation fidelity exceeding 99%, Sci. Adv. **8**, eabn5130 (2022).

[27] A. Noiri, K. Takeda, T. Nakajima, T. Kobayashi, A. Sammak, G. Scappucci, and S. Tarucha, Fast universal quantum gate above the fault-tolerance threshold in silicon, Nature **601**, 338 (2022).

[28] X. Xue, M. Russ, N. Samkharadze, B. Undseth, A. Sammak, G. Scappucci, and L. M. K. Vandersypen, Quantum logic with spin qubits crossing the surface code threshold, Nature **601**, 343 (2022).

[29] M. T. Mądzik, S. Asaad, A. Youssry, B. Joecker, K. M. Rudinger, E. Nielsen, K. C. Young, T. J. Proctor, A. D. Baczewski, A. Laucht, V. Schmitt, F. E. Hudson, K. M. Itoh, A. M. Jakob, B. C. Johnson, D. N. Jamieson, A. S. Dzurak, C. Ferrie, R. Blume-Kohout, and A. Morello, Precision tomography of a three-qubit donor quantum processor in silicon, Nature **601**, 348 (2022).

[30] I. N. Moskalenko, I. A. Simakov, N. N. Abramov, A. A. Grigorev, D. O. Moskalev, A. A. Pishchimova, N. S. Smirnov, E. V. Zikiy, I. A. Rodionov, and I. S. Besedin, High fidelity two-qubit gates on fluxoniums using a tunable coupler, npj Quantum Inf. **8**, 130 (2022).

[31] A. Kandala, K. X. Wei, S. Srinivasan, E. Magesan, S. Carnevale, G. A. Keefe, D. Klaus, O. Dial, and D. C. McKay, Demonstration of a high-fidelity cnot gate for fixed-frequency transmons with engineered *zz* suppression, Phys. Rev. Lett. **127**, 130501 (2021).

[32] Y. Sung, L. Ding, J. Braumüller, A. Vepsäläinen, B. Kannan, M. Kjaergaard, A. Greene, G. O. Samach, C. McNally, D. Kim, A. Melville, B. M. Niedzielski, M. E. Schwartz, J. L. Yoder, T. P. Orlando, S. Gustavsson, and W. D. Oliver, Realization of high-fidelity CZ and *ZZ*-free iswap gates with a tunable coupler, Phys. Rev. X **11**, 021058 (2021).

[33] I. S. Madjarov, J. P. Covey, A. L. Shaw, J. Choi, A. Kale, A. Cooper, H. Pichler, V. Schkolnik, J. R. Williams, and M. Endres, High-fidelity entanglement and detection of alkaline-earth Rydberg atoms, Nat. Phys. **16**, 857 (2020).

[34] S. J. Evered, D. Bluvstein, M. Kalinowski, S. Ebadi, T. Manovitz, H. Zhou, S. H. Li, A. A. Geim, T. T. Wang, N. Maskara, H. Levine, G. Semeghini, M. Greiner, V. Vuletić, and M. D. Lukin, High-fidelity parallel entangling gates on a neutral-atom quantum computer, Nature **622**, 268 (2023).

[35] P. Scholl, A. L. Shaw, R. B.-S. Tsai, R. Finkelstein, J. Choi, and M. Endres, Erasure conversion in a high-fidelity Rydberg quantum simulator, Nature **622**, 273 (2023).

[36] Y. Wang, S. Crain, C. Fang, B. Zhang, S. Huang, Q. Liang, P. H. Leung, K. R. Brown, and J. Kim, High-fidelity two-qubit gates using a microelectromechanical-system-based beam steering system for individual qubit addressing, Phys. Rev. Lett. **125**, 150505 (2020).

[37] C. J. Ballance, T. P. Harty, N. M. Linke, M. A. Sepiol, and D. M. Lucas, High-fidelity quantum logic gates using trapped-ion hyperfine qubits, Phys. Rev. Lett. **117**, 060504 (2016).

[38] C. R. Clark, H. N. Tinkey, B. C. Sawyer, A. M. Meier, K. A. Burkhardt, C. M. Seck, C. M. Shappert, N. D. Guise, C. E. Volin, S. D. Fallek, H. T. Hayden, W. G. Rellergert, and K. R. Brown, High-fidelity bell-state preparation with $^{40}Ca^{+}$ optical qubits, Phys. Rev. Lett. **127**, 130505 (2021).

[39] E. Nielsen, J. K. Gamble, K. Rudinger, T. Scholten, K. Young, and R. Blume-Kohout, Gate set tomography, Quantum **5**, 557 (2021).

[40] R. Blume-Kohout, M. P. da Silva, E. Nielsen, T. Proctor, K. Rudinger, M. Sarovar, and K. Young, A taxonomy of small Markovian errors, PRX Quantum **3**, 020335 (2022).

[41] M. J. Degen, S. J. H. Loenen, H. P. Bartling, C. E. Bradley, A. L. Meinsma, M. Markham, D. J. Twitchen, and T. H. Taminiau, Entanglement of dark electron-nuclear spin defects in diamond, Nat. Commun. **12**, 3470 (2021).

[42] C. E. Bradley, S. W. de Bone, P. F. W. Möller, S. Baier, M. J. Degen, S. J. H. Loenen, H. P. Bartling, M. Markham, D. J. Twitchen, R. Hanson, D. Elkouss, and T. H. Taminiau, Robust quantum-network memory based on spin qubits in isotopically engineered diamond, npj Quantum Inf. **8**, 122 (2022).

[43] M. W. Doherty, F. Dolde, H. Fedder, F. Jelezko, J. Wrachtrup, N. B. Manson, and L. C. L. Hollenberg, Theory of the ground-state spin of the NV^{-} center in diamond, Phys. Rev. B **85**, 205203 (2012).

[44] See Supplemental Material at http://link.aps.org/supplemental/10.1103/PhysRevApplied.23.034052 for details on the experimental setup, the Hamiltonian of the system, and additional gate set tomography results.

[45] L. Robledo, L. Childress, H. Bernien, B. Hensen, P. F. A. Alkemade, and R. Hanson, High-fidelity projective readout of a solid-state spin quantum register, Nature **477**, 574 (2011).

[46] H. Bernien, B. Hensen, W. Pfaff, G. Koolstra, M. S. Blok, L. Robledo, T. H. Taminiau, M. Markham, D. J. Twitchen, L. Childress, and R. Hanson, Heralded entanglement between solid-state qubits separated by three metres, Nature **497**, 86 (2013).

[47] R. Blume-Kohout, J. K. Gamble, E. Nielsen, K. Rudinger, J. Mizrahi, K. Fortier, and P. Maunz, Demonstration of qubit operations below a rigorous fault tolerance threshold with gate set tomography, Nat. Commun. **8**, 14485 (2017).

[48] T. Proctor, M. Revelle, E. Nielsen, K. Rudinger, D. Lobser, P. Maunz, R. Blume-Kohout, and K. Young, Detecting and tracking drift in quantum information processors, Nat. Commun. **11**, 5396 (2020).

[49] J. P. Dehollain, J. T. Muhonen, R. Blume-Kohout, K. M. Rudinger, J. K. Gamble, E. Nielsen, A. Laucht, S. Simmons, R. Kalra, A. S. Dzurak, and A. Morello, Optimization of a solid-state electron spin qubit using gate set tomography, New J. Phys. **18**, 103018 (2016).

[50] G. White, C. Hill, and L. Hollenberg, Performance optimization for drift-robust fidelity improvement of two-qubit gates, Phys. Rev. Appl. **15**, 014023 (2021).

[51] J. Emerson, R. Alicki, and K. Życzkowski, Scalable noise estimation with random unitary operators, J. Opt. B: Quantum Semiclassical Opt. **7**, S347 (2005).

[52] E. Magesan, R. Blume-Kohout, and J. Emerson, Gate fidelity fluctuations and quantum process invariants, Phys. Rev. A **84**, 012309 (2011).

[53] J. Helsen, I. Roth, E. Onorati, A. Werner, and J. Eisert, General framework for randomized benchmarking, PRX Quantum **3**, 020357 (2022).

[54] J. J. Wallman and S. T. Flammia, Randomized benchmarking with confidence, New J. Phys. **16**, 103032 (2014).

[55] T. Proctor, K. Rudinger, K. Young, M. Sarovar, and R. Blume-Kohout, What randomized benchmarking actually measures, Phys. Rev. Lett. **119**, 130502 (2017).

[56] J. M. Epstein, A. W. Cross, E. Magesan, and J. M. Gambetta, Investigating the limits of randomized benchmarking protocols, Phys. Rev. A **89**, 062321 (2014).

[57] E. Magesan, J. M. Gambetta, B. R. Johnson, C. A. Ryan, J. M. Chow, S. T. Merkel, M. P. da Silva, G. A. Keefe, M. B. Rothwell, T. A. Ohki, M. B. Ketchen, and M. Steffen,

Efficient measurement of quantum gate error by interleaved randomized benchmarking, Phys. Rev. Lett. **109**, 080505 (2012).

[58] S. Sheldon, L. S. Bishop, E. Magesan, S. Filipp, J. M. Chow, and J. M. Gambetta, Characterizing errors on qubit operations via iterative randomized benchmarking, Phys. Rev. A **93**, 012301 (2016).

[59] S. Boixo, S. V. Isakov, V. N. Smelyanskiy, R. Babbush, N. Ding, Z. Jiang, M. J. Bremner, J. M. Martinis, and H. Neven, Characterizing quantum supremacy in near-term devices, Nat. Phys. **14**, 595 (2018).

[60] F. Arute *et al.*, Quantum supremacy using a programmable superconducting processor, Nature **574**, 505 (2019).

[61] T. H. Taminiau, J. J. T. Wagenaar, T. van der Sar, F. Jelezko, V. V. Dobrovitski, and R. Hanson, Detection and control of individual nuclear spins using a weakly coupled electron spin, Phys. Rev. Lett. **109**, 137602 (2012).

[62] S. Kolkowitz, Q. P. Unterreithmeier, S. D. Bennett, and M. D. Lukin, Sensing distant nuclear spins with a single electron spin, Phys. Rev. Lett. **109**, 137601 (2012).

[63] M. H. Abobeih, J. Cramer, M. A. Bakker, N. Kalb, M. Markham, D. J. Twitchen, and T. H. Taminiau, One-second coherence for a single electron spin coupled to a multi-qubit nuclear-spin environment, Nat. Commun. **9**, 2552 (2018).

[64] H. P. Bartling, M. H. Abobeih, B. Pingault, M. J. Degen, S. J. H. Loenen, C. E. Bradley, J. Randall, M. Markham, D. J. Twitchen, and T. H. Taminiau, Entanglement of spin-pair qubits with intrinsic dephasing times exceeding a minute, Phys. Rev. X **12**, 011048 (2022).

[65] H. P. Bartling, N. Demetriou, N. C. F. Zutt, D. Kwiatkowski, M. J. Degen, S. J. H. Loenen, C. E. Bradley, M. Markham, D. J. Twitchen, and T. H. Taminiau, Control of individual electron-spin pairs in an electron-spin bath, arXiv:2311.10110 [quant-ph].

[66] Y.-X. Liu, A. Ajoy, and P. Cappellaro, Nanoscale vector dc magnetometry via ancilla-assisted frequency up-conversion, Phys. Rev. Lett. **122**, 100501 (2019).

[67] M. A. Nielsen, A simple formula for the average gate fidelity of a quantum dynamical operation, Phys. Lett. A **303**, 249 (2002).

[68] Y. R. Sanders, J. J. Wallman, and B. C. Sanders, Bounding quantum gate error rate based on reported average fidelity, New J. Phys. **18**, 012002 (2015).

[69] T. P. Harty, D. T. C. Allcock, C. J. Ballance, L. Guidoni, H. A. Janacek, N. M. Linke, D. N. Stacey, and D. M. Lucas, High-fidelity preparation, gates, memory, and readout of a trapped-ion quantum bit, Phys. Rev. Lett. **113**, 220501 (2014).

[70] A. D. Leu, M. F. Gely, M. A. Weber, M. C. Smith, D. P. Nadlinger, and D. M. Lucas, Fast, high-fidelity addressed single-qubit gates using efficient composite pulse sequences, Phys. Rev. Lett. **131**, 120601 (2023).

[71] R. Barends *et al.*, Superconducting quantum circuits at the surface code threshold for fault tolerance, Nature **508**, 500 (2014).

[72] C. H. Yang, K. W. Chan, R. Harper, W. Huang, T. Evans, J. C. C. Hwang, B. Hensen, A. Laucht, T. Tanttu, F. E. Hudson, S. T. Flammia, K. M. Itoh, A. Morello, S. D. Bartlett, and A. S. Dzurak, Silicon qubit fidelities approaching incoherent noise limits via pulse engineering, Nat. Electron. **2**, 151 (2019).

[73] J. Yoneda, K. Takeda, T. Otsuka, T. Nakajima, M. R. Delbecq, G. Allison, T. Honda, T. Kodera, S. Oda, Y. Hoshi, N. Usami, K. M. Itoh, and S. Tarucha, A quantum-dot spin qubit with coherence limited by charge noise and fidelity higher than 99.9%, Nat. Nanotechnol. **13**, 102 (2018).

[74] O. Kern, G. Alber, and D. L. Shepelyansky, Quantum error correction of coherent errors by randomization, Eur. Phys. J. D **32**, 153 (2005).

[75] J. J. Wallman and J. Emerson, Noise tailoring for scalable quantum computation via randomized compiling, Phys. Rev. A **94**, 052325 (2016).

[76] R. Nagy, M. Niethammer, M. Widmann, Y.-C. Chen, P. Udvarhelyi, C. Bonato, J. U. Hassan, R. Karhu, I. G. Ivanov, N. T. Son, J. R. Maze, T. Ohshima, Ö. O. Soykal, Á. Gali, S.-Y. Lee, F. Kaiser, and J. Wrachtrup, High-fidelity spin and optical control of single silicon-vacancy centres in silicon carbide, Nat. Commun. **10**, 1954 (2019).

[77] B. Pingault, D.-D. Jarausch, C. Hepp, L. Klintberg, J. N. Becker, M. Markham, C. Becher, and M. Atatüre, Coherent control of the silicon-vacancy spin in diamond, Nat. Commun. **8**, 15579 (2017).

[78] E. I. Rosenthal, C. P. Anderson, H. C. Kleidermacher, A. J. Stein, H. Lee, J. Grzesik, G. Scuri, A. E. Rugar, D. Riedel, S. Aghaeimeibodi, G. H. Ahn, K. Van Gasse, and J. Vučković, Microwave spin control of a tin-vacancy qubit in diamond, Phys. Rev. X **13**, 031022 (2023).

[79] Delft High Performance Computing Centre (DHPC), DelftBlue Supercomputer (Phase 1), https://www.tudelft.nl/dhpc/ark:/44463/DelftBluePhase1 (2023).

[80] H. P. Bartling, J. Yun, K. N. Schymik, M. van Riggelen, L. A. Enthoven, H. B. van Ommen, M. Babaie, F. Sebastiano, M. Markham, D. J. Twitchen, and T. H. Taminiau, Data for universal high-fidelity quantum gates for spin-qubits in diamond, 4TU.ResearchData (2025).

[81] M. H. Abobeih, J. Randall, C. E. Bradley, H. P. Bartling, M. A. Bakker, M. J. Degen, M. Markham, D. J. Twitchen, and T. H. Taminiau, Atomic-scale imaging of a 27-nuclear-spin cluster using a quantum sensor, Nature **576**, 411 (2019).

[82] Pygsti, http://www.pygsti.info/.

[83] J. M. Chow, J. M. Gambetta, A. D. Córcoles, S. T. Merkel, J. A. Smolin, C. Rigetti, S. Poletto, G. A. Keefe, M. B. Rothwell, J. R. Rozen, M. B. Ketchen, and M. Steffen, Universal quantum gate set approaching fault-tolerant thresholds with superconducting qubits, Phys. Rev. Lett. **109**, 060501 (2012).

[84] G. Balasubramanian, I. Y. Chan, R. Kolesov, M. Al-Hmoud, J. Tisler, C. Shin, C. Kim, A. Wojcik, P. R. Hemmer, A. Krueger, T. Hanke, A. Leitenstorfer, R. Bratschitsch, F. Jelezko, and J. Wrachtrup, Nanoscale imaging magnetometry with diamond spins under ambient conditions, Nature **455**, 648 (2008).

[85] T. H. Taminiau, J. Cramer, T. van der Sar, V. V. Dobrovitski, and R. Hanson, Universal control and error correction in multi-qubit spin registers in diamond, Nat. Nanotechnol. **9**, 171 (2014).

[86] W. S. Warren, Effects of arbitrary laser or nmr pulse shapes on population inversion and coherence, J. Chem. Phys. **81**, 5437 (1984).

[87] L. M. Vandersypen and I. L. Chuang, NMR techniques for quantum control and computation, Rev. Mod. Phys. **76**, 1037 (2005).

[88] B. Nachman, M. Urbanek, W. A. de Jong, and C. W. Bauer, Unfolding quantum computer readout noise, npj Quantum Inf. **6**, 84 (2020).

[89] J. J. Wallman, Randomized benchmarking with gate-dependent noise, Quantum **2**, 47 (2018).

[90] Y. Li and S. C. Benjamin, Efficient variational quantum simulator incorporating active error minimization, Phys. Rev. X **7**, 021050 (2017).

[91] K. Temme, S. Bravyi, and J. M. Gambetta, Error mitigation for short-depth quantum circuits, Phys. Rev. Lett. **119**, 180509 (2017).

[92] S. Endo, S. C. Benjamin, and Y. Li, Practical quantum error mitigation for near-future applications, Phys. Rev. X **8**, 031027 (2018).

[93] Y. Kim, A. Eddins, S. Anand, K. X. Wei, E. van den Berg, S. Rosenblatt, H. Nayfeh, Y. Wu, M. Zaletel, K. Temme, and A. Kandala, Evidence for the utility of quantum computing before fault tolerance, Nature **618**, 500 (2023).

[94] J. R. Johansson, P. D. Nation, and F. Nori, QuTiP: An open-source Python framework for the dynamics of open quantum systems, Comput. Phys. Commun. **183**, 1760 (2012).

[95] J. R. Johansson, P. D. Nation, and F. Nori, QuTiP 2: A Python framework for the dynamics of open quantum systems, Comput. Phys. Commun. **184**, 1234 (2013).

[96] K. M. Rudinger, C. I. Ostrove, S. K. Seritan, M. D. Grace, E. Nielsen, R. J. Blume-Kohout, and K. C. Young, Two-qubit gate set tomography with fewer circuits, arXiv:2307.15767 [quant-ph].